

Supercritical accretion of stellar-mass compact objects in active galactic nuclei

ZHEN PAN¹ AND HUAN YANG^{1,2}

¹*Perimeter Institute for Theoretical Physics, Waterloo, Ontario N2L 2Y5, Canada*

²*University of Guelph, Guelph, Ontario N1G 2W1, Canada*

Submitted to ApJ

ABSTRACT

Accretion disks of active galactic nuclei (AGN) have been proposed as promising sites for producing both (stellar-mass) compact object mergers and extreme mass ratio inspirals. Along with the disk-assisted migration/evolution process, ambient gas materials inevitably accrete onto the compact objects. The description of this process is subject to significant theoretical uncertainties in previous studies. It was commonly assumed that either an Eddington accretion rate or a Bondi accretion rate (or any rate in between) takes place, although these two rates can differ from each other by several orders of magnitude. As a result, the mass and spin evolution of compact objects within AGN disks are essentially unknown. In this work, we construct a relativistic supercritical inflow-outflow model for black hole (BH) accretion. We show that the radiation efficiency of the supercritical accretion of a stellar-mass BH (sBH) is generally too low to explain the proposed electromagnetic counterpart of GW190521. Applying this model to sBHs embedded in AGN disks, we find that, although the gas inflow rates at Bondi radii of these sBHs are in general highly super-Eddington, a large fraction of inflowing gas eventually escapes as outflows so that only a small fraction accretes onto the sBH, resulting in mildly super-Eddington BH absorption in most cases. We also implement this inflow-outflow model to study the evolution of neutron stars (NS) and white dwarfs (WD) in AGN disks, taking into account corrections from star sizes and star magnetic fields. It turns out to be difficult for WDs to grow to the Chandrasekhar limit via accretion because WDs are spun up more efficiently to reach the shedding limit before the Chandrasekhar limit. For NSs the accretion-induced collapse is possible if NS magnetic fields are sufficiently strong to guide the accretion flow outside the NS surface, keeping the NS in a slow rotation state during the whole accretion process.

Keywords: Active galactic nuclei(16); Black holes(162); Bondi accretion(174); Gravitational waves (678)

1. INTRODUCTION

With a growing catalog of binary black holes, binary neutron stars and black hole-neutron star systems detected by Advanced LIGO and Virgo, in recent years extensive studies have been conducted on their possible formation channels (LIGO Scientific Collaboration & Virgo Collaboration 2021). In addition to isolated binaries (e.g. Portegies Zwart & McMillan 2000; Hurley et al. 2002; Belczynski et al. 2002) and dynamical formation in dense stellar clusters (e.g. Sigurdsson & Phinney 1993; Lee 1995; Portegies Zwart & McMillan 2000; Banerjee et al. 2010; Stephan et al. 2016; Bartos et al. 2017), binary formation in accretion disks of

active galactic nuclei (AGN) has been proposed as another promising and interesting channel (Stone et al. 2017; Bartos et al. 2017; McKernan et al. 2018; Leigh et al. 2018; Yang et al. 2019a,b, 2020b,a; Secunda et al. 2019, 2020; McKernan et al. 2020a,b). The gas-rich environment is expected to leave unique observational signatures on mergers of stellar-mass compact objects in AGN disks. For example, binary black hole (BBH) mergers in AGN disks may generate detectable electromagnetic (EM) signals (McKernan et al. 2019; Graham et al. 2020; Kimura et al. 2021; Wang et al. 2021b) which should be absent in other formation channels; gamma-ray bursts arising from binary neutron star (BNS) mergers in AGN disks may also yield different EM signals and detectable high-energy neutrino emission (Kimura et al. 2021; Perna et al. 2021a; Zhu et al. 2021a,b,d). During the entire inspiral stage, gas accretion onto these compact objects may

change their masses and spins, e.g., producing compact objects within the lower and upper mass gaps, and compact binaries with non-zero effective spins (McKernan et al. 2020b; Yang et al. 2020b; Tagawa et al. 2020a,b, 2021; Gilbaum & Stone 2021).

Besides forming binaries and eventually produce coalescence gravitational wave signals in the frequency band of ground-based detectors, compact objects embedded in AGN disk give rise to plenty of other interesting phenomena. For example, stellar-mass BHs (sBHs) may be captured by AGN disks and then migrate inward to the galactic-center, massive BH (MBH), which has been suggested as an important or even dominant formation channel of extreme mass ratio inspirals (EMRIs) (Pan & Yang 2021; Pan et al. 2021) based on the rate calculations, so that they belong to the primary targets for the laser interferometer space antenna (LISA) with possible environmental waveform characteristics (Bonga et al. 2019; Yang & Casals 2017; Yang et al. 2019; Yunes et al. 2011); the birth and growth of intermediate-mass black holes in AGN disks have been investigated (McKernan et al. 2012, 2014); observation prospects of accretion onto compact objects and accretion induced collapses of neutron stars (NSs) and white dwarfs (WDs) in AGN disks have also been discussed in detail (Wang et al. 2021a; Perna et al. 2021b; Zhu et al. 2021c).

On the other hand, the accretion onto compact objects in AGN disks plays an essential role in determining the mass and spin evolution of these objects. Straight estimation using the Bondi accretion formula (without considering possible outflows) suggests that the accretion is highly supercritical, the rate of which is usually many orders of magnitude higher than the Eddington accretion rate. In previous studies (e.g., McKernan et al. 2020b; Yang et al. 2020b; Tagawa et al. 2020a,b, 2021; Gilbaum & Stone 2021), an Eddington accretion rate or a Bondi accretion rate is usually assumed, which makes model predictions that are sensitive to the accretion rate highly uncertain. As shown in many analytic models (Blandford & Begelman 1999, 2004; Begelman 2012) and numerical simulations (Yuan et al. 2012a,b; Sadowski et al. 2014; McKinney et al. 2014; Yang et al. 2014; Takahashi et al. 2018), outflow naturally emerges in cases of supercritical accretion of compact objects, such that only a (small) fraction of inflowing gas at the outer boundary finally accretes onto the central compact object. In this paper, we aim to build a relativistic supercritical inflow-outflow model of BHs and apply this model to study the mass and spin evolution of sBHs embedded in AGN disks, along with EM emissions. Given a mass inflow rate at outer boundary, all the flow properties, including the disk structure, radiation cooling rate and the accretion rate onto the sBH, are uniquely determined within the supercritical inflow-outflow model. We find supercritical accretion flows are in general radiation in-

efficient and advection dominated, similar to the well-known advection dominated accretion flows (ADAFs) (Narayan & Yi 1994; Narayan et al. 1997). In particular, it is unlikely to explain the proposed bright EM counterpart of GW190521, if it indeed originated from the same BBH system (see also Ashton et al. 2020; Nitz & Capano 2021; Palmese et al. 2021), by supercritical accretion of the remnant BH in an AGN disk as claimed in Graham et al. (2020).

After applying this supercritical accretion model on sBHs embedded in AGN disks, we find that the gas inflow rate at the outer boundary r_{obd} , where the infalling gas circularizes into a disk profile, is in general highly super-Eddington, i.e., $\dot{m}_*(r_{\text{obd}}) \gg \dot{m}_*^{\text{Edd}}$. A large fraction of inflowing gas escapes as outflow and only a small fraction gets accreted by the central sBH, and the accretion onto sBHs turns out to be mildly super-Eddington in most cases, i.e., $\dot{m}_{*,0} \gtrsim \dot{m}_*^{\text{Edd}}$. As a result, the majority of sBHs that are captured onto the AGN disk and migrate into the MBH within the AGN disk lifetime only grow by a small fraction due to accretion, and the majority of the mass accumulation happens in the vicinity of the central MBH, where the gas density is high. We also calculate the spatial distribution of sBHs captured into the disk, which suggests that $\approx (5 - 50)$ sBHs aggregate around the MBH within 10^3 times the MBH gravitational radius, depending on the disk model and the disk lifetime. It has an interesting implication for sBHs in Sgr A*: a number of sBHs should be brought to the vicinity of the galactic MBH during its previous AGN phase, $\approx (2 - 12)$ of which are expected to be still orbiting around the Sgr A* today if the AGN phase happened in less than 10 Myr ago. These remaining sBHs may be promising monochromatic sources detectable by LISA.

For WDs embedded in AGN disks, the accretion rates are usually higher than that of BHs of similar mass because of much larger star sizes. However, WDs are spun up more efficiently to the shedding limit before reaching the Chandrasekhar limit, so that it is hard for WDs to reach the Chandrasekhar limit via accretion. On the other hand, it is possible for NSs to grow to the collapse limit via accretion if NS magnetic fields are sufficiently strong to guide the accretion flow outside the NS surface and consequently keep the NS in a slow rotation state while accreting gas. This is a natural way of forming mass-gap-EMRIs in which stellar-mass compact objects are more massive than the heaviest NSs but lighter than $\sim 5M_{\odot}$.

This paper is organized as follows. In Section 2, we construct a relativistic model of supercritical accretion of BHs, based on which we study the claimed EM counterpart of GW190521. In Sections 3 and 4, we apply the supercritical inflow-outflow model on studying evolution of sBHs, NSs and WDs in AGN disks, respectively. We summarize this paper in Section 5. Throughout this paper, we use geometrical units $G = c = 1$.

2. SUPERCRITICAL INFLOW-OUTFLOW MODEL

In this section, we start with a brief review of the supercritical inflow-outflow model in Newtonian gravity proposed by Blandford and Begelman (Blandford & Begelman 1999, 2004; Begelman 2012). After that we extend the model to the Kerr spacetime, obtain numerical solutions in the relativistic regime, and finally discuss its application in explaining the EM counterpart of GW190521.

2.1. Newtonian model

In the context of supercritical accretion onto a compact object with mass m_\bullet , part of the inflow gas escapes in the form of outflow, thus the gas inflow rate $\dot{m}_{\text{in}}(r)$ increases with radius r . The dynamics of steady inflow is governed by the Eulerian equation, the angular momentum equation and the energy equation (Begelman 2012):

$$v_r \frac{\partial v_r}{\partial r} = \frac{v_\phi^2}{r} - \frac{m_\bullet}{r^2} - \frac{1}{\rho} \frac{\partial p}{\partial r}, \quad (1a)$$

$$\frac{\partial}{\partial r}(T - \dot{m}_{\text{in}}L) = -(1 + \eta_1)L \frac{\partial \dot{m}_{\text{in}}}{\partial r}, \quad (1b)$$

$$\frac{\partial}{\partial r}(T\Omega - \dot{m}_{\text{in}}B) = -(1 - \eta_2)B \frac{\partial \dot{m}_{\text{in}}}{\partial r} - 2\pi r F^-, \quad (1c)$$

where v_r and v_ϕ are the velocity in the r and ϕ directions, respectively; p and ρ are the gas pressure and the gas density, respectively; $L(r) = rv_\phi = r^2\Omega$ is the specific angular momentum; $B(r) = \frac{v_r^2 + v_\phi^2}{2} - \frac{m_\bullet}{r} + \frac{\Gamma}{\Gamma-1} \frac{p}{\rho}$ is the Bernoulli parameter for the inflow material with Γ being the adiabatic index, which we take as $\Gamma = 4/3$; $F^-(r) = 2\sigma_{\text{SB}}T_{\text{eff}}^4$ is the energy flux of radiation cooling from both surfaces of the disk with T_{eff} being the effective temperature; $T(r) = -2\pi r^2 \cdot (2H \cdot \nu \rho r \frac{\partial \Omega}{\partial r})$ is the torque that the part of disk with radius $\leq r$ exerts on the exterior part, with ν being the viscosity coefficient relating to the local sound speed c_s and the disk height via $\nu = \frac{2}{3}\alpha c_s H$ following the commonly used α prescription (Shakura & Sunyaev 1973); $\eta_{1,2}$ measures the difference of the specific angular momentum (energy) carried by gas that turns around from inflow to outflow relative to that of gas still in the inflow at the same radius, and we take $\eta_1 = \eta_2 = 0$ considering that there should be no discontinuity between the two (see e.g., Xie & Yuan 2008; Zahra Zeraatgari et al. 2016, for the impact of non-zero $\eta_{1,2}$).

The three dynamical equations above are supplemented by the following constraint equations:

$$\Sigma = 2\rho H, \quad (2a)$$

$$-2\pi r \Sigma v_r = \dot{m}_{\text{in}}(r), \quad (2b)$$

$$c_s^2 = \frac{m_\bullet}{r^3} H^2, \quad (2c)$$

$$p = \rho c_s^2 \quad (2d)$$

$$T_{\text{mid}}^4 = \left(\frac{3}{8}\tau + \frac{1}{2} + \frac{1}{4\tau} \right) T_{\text{eff}}^4, \quad (2e)$$

$$\tau = \frac{\kappa \Sigma}{2}, \quad (2f)$$

$$p = p_{\text{rad}} + p_{\text{gas}} \quad (2g)$$

$$p_{\text{rad}} = \frac{\tau}{2} \sigma_{\text{SB}} T_{\text{eff}}^4, \quad (2h)$$

$$p_{\text{gas}} = \frac{\rho}{m_p} k_B T_{\text{mid}}, \quad (2i)$$

where m_p is the proton mass, k_B is the Boltzmann constant, Σ is the surface density, T_{mid} is the middle plane temperature, τ is the optical depth, $\kappa = \kappa_{\text{sct}} + \kappa_{\text{abs}}$ is the gas opacity contributed by electron scattering and free-free absorption with $\kappa_{\text{sct}} = 0.34 \text{ cm}^2/\text{g}$, and $\kappa_{\text{abs}} = 1.7 \times 10^{-25} (T_{\text{mid}}/\text{K})^{-7/2} (\rho/(\text{cm}^3 \text{g}^{-1})) (m_p/\text{g})^{-2} \text{ cm}^2/\text{g}$ (Rybicki & Lightman 1986).

To close the equations above, one more prescription for the inflow rate $\dot{m}_{\text{in}}(r)$ is needed. As shown in Begelman (2012), the condition

$$\dot{m}_{\text{in}}(r)B(r) \approx \text{const}, \quad (3)$$

must be satisfied to ensure that the Bernoulli parameter of the inflow is bounded from that of the outflow ($B < B_{\text{out}}$) everywhere¹.

In inner parts where $p_{\text{rad}} > p_{\text{gas}}$ and $\kappa_{\text{sct}} > \kappa_{\text{abs}}$, there exists a unique self-similar solution to the equations above with $\dot{m}_{\text{in}} \propto r$, $\rho \propto r^{-1/2}$, $p \propto r^{-3/2}$, $H \propto r$, $v_r \propto r^{-1/2}$, $c_s \propto r^{-1/2}$, $\Omega \propto r^{-3/2}$ and $T_{\text{mid}} \propto r^{-3/8}$, $T_{\text{eff}} \propto r^{-1/2}$ (Begelman 2012; Zahra Zeraatgari et al. 2016, 2020). The self-similar solution in Newtonian gravity is consistent with numerical simulation results (Yuan et al. 2012a,b; Sadowski et al. 2014; McKinney et al. 2014; Yang et al. 2014; Takahashi et al. 2018) for $r \gtrsim 10m_\bullet$. Similar to ADAFs (Narayan & Yi 1994; Narayan et al. 1997), the supercritical inflow is radiation inefficient and advection dominated.² In outer parts where $p_{\text{rad}} < p_{\text{gas}}$ and/or $\kappa_{\text{sct}} < \kappa_{\text{abs}}$, the supercritical inflow becomes even more advection dominated and the radiation cooling is negligible. In this case, there is no exact self-similar solution, and we can approximately write the solution as: $\dot{m}_{\text{in}} \propto r$, $\rho \propto r^{-1/2}$, $p \propto r^{-3/2}$, $H \propto r$, $v_r \propto r^{-1/2}$, $c_s \propto r^{-1/2}$, $\Omega \propto r^{-3/2}$ and $T_{\text{mid}} \propto r^{-1}$, $T_{\text{eff}} \propto r^{-9/8}$ accurate to

¹ B_{out} can be obtained using the energy and angular momentum conservation equations for the outflows, as explained in Begelman (2012)

² We thank Prof. Feng Yuan for pointing out this similarity.

$O(\ln r/r)$. In outer most parts, the disk becomes unstable due to self-gravity, where the Toomre's stability parameter

$$Q := \frac{c_s \Omega}{\pi \Sigma} \quad (4)$$

becomes less than unity, and we denote the marginally stable radius where $Q = 1$ as r_Q .

2.2. General Relativistic model

Following Abramowicz et al. (1996), we extend the above inflow-outflow model to the relativistic regime, with the background spacetime being Kerr. In the vicinity of the equatorial plane, the Kerr metric is approximately (Page & Thorne 1974)

$$\begin{aligned} ds^2 &= g_{tt} dt^2 + 2g_{t\phi} dt d\phi + g_{\phi\phi} d\phi^2 + g_{rr} dr^2 + g_{zz} dz^2, \\ &= -\frac{r^2 \Delta}{A} dt^2 + \frac{A}{r^2} (d\phi - \omega dt)^2 + \frac{r^2}{\Delta} dr^2 + dz^2, \end{aligned} \quad (5)$$

with

$$\Delta = r^2 - 2m_\bullet r + a^2, \quad A = r^4 + r^2 a^2 + 2m_\bullet r a^2, \quad \omega = \frac{2m_\bullet a r}{A}.$$

Assuming the four-velocity of matter has three non-vanishing components

$$u^\mu = (u^t, u^r, 0, u^\phi), \quad (6)$$

we define the angular velocity Ω relative to the stationary observer and the angular velocity $\tilde{\Omega}$ relative to the local inertial observer by

$$\Omega = \frac{u^\phi}{u^t}, \quad \tilde{\Omega} = \Omega - \omega. \quad (7)$$

In particular, the angular velocity of the corotating and counterrotating Keplerian orbits are

$$\Omega_\pm = \pm \frac{m_\bullet^{1/2}}{r^{3/2} \pm a m_\bullet^{1/2}}. \quad (8)$$

In accordance with Abramowicz et al. (1996), we define a rescaled radial velocity V by

$$\frac{V}{\sqrt{1-V^2}} = u^r \sqrt{g_{rr}}, \quad (9)$$

and the Lorentz factors of the total motion γ and of the ϕ -direction motion γ_ϕ

$$\gamma = \frac{1}{\sqrt{1 - \tilde{\Omega}^2 \tilde{R}^2}} \frac{1}{\sqrt{1 - V^2}}, \quad \gamma_\phi = \frac{1}{\sqrt{1 - \tilde{\Omega}^2 \tilde{R}^2}}, \quad (10)$$

with $\tilde{R}^2 = \frac{A^2}{r^4 \Delta}$. As a result, the specific angular momentum and the specific energy are given by

$$L = \gamma \frac{A^{3/2}}{r^3 \Delta^{1/2}} \tilde{\Omega}, \quad E = -\frac{g_{tt} + g_{t\phi} \Omega}{g_{t\phi} + g_{\phi\phi} \Omega} L. \quad (11)$$

With the definitions above, the three dynamical equations in Eq. (1) written in the relativistic form become

$$\frac{1}{1-V^2} \frac{V^2}{c_s^2} \frac{\partial \ln V}{\partial \ln r} = \frac{\mathcal{A}}{c_s^2} - \frac{\partial \ln \rho}{\partial \ln r} - 2 \frac{\partial \ln c_s}{\partial \ln r}, \quad (12a)$$

$$\frac{1}{2\pi} \left[(\dot{m}_{\text{in}} L - \dot{m}_{\text{in},0} L_0) - \int_{r_0}^r L \frac{d\dot{m}_{\text{in}}}{dr} dr \right] = -v \frac{\Sigma A^{3/2} \Delta^{1/2} \gamma^3}{r^4} \frac{\partial \Omega}{\partial r}, \quad (12b)$$

$$\dot{m}_{\text{in}} \left(\frac{1}{\Gamma - 1} \frac{\partial c_s^2}{\partial \ln r} - c_s^2 \frac{\partial \ln \rho}{\partial \ln r} \right) = -2\pi r^2 (F^+ - F^-), \quad (12c)$$

with

$$\mathcal{A} = -\frac{m_\bullet A}{r^3 \Delta \Omega_+ \Omega_-} \frac{(\Omega - \Omega_+)(\Omega - \Omega_-)}{1 - \tilde{\Omega}^2 \tilde{R}^2},$$

where $\dot{m}_{\text{in},0}$ is the gas inflow rate on the horizon, L_0 is the specific angular momentum of gas on the horizon, the viscosity heating rate is given by $F^+ = v \Sigma \gamma^4 \left(\frac{A}{r^3} \frac{\partial \Omega}{\partial r} \right)^2$ and the radiation cooling rate is $F^- = 2\sigma_{\text{SB}} T_{\text{eff}}^4$.

Similar to Eq. (2), the constraint equations in the relativistic form are

$$\Sigma = 2\rho H \quad (13a)$$

$$-2\pi \Sigma \sqrt{\Delta} \frac{V}{\sqrt{1-V^2}} = \dot{m}_{\text{in}}(r) \quad (13b)$$

$$c_s = \gamma H \sqrt{\frac{m_\bullet (r^2 + a^2)^2 + 2\Delta a^2}{r^3 (r^2 + a^2)^2 - \Delta a^2}} := \gamma H \Omega_\perp, \quad (13c)$$

$$p = \rho c_s^2 \quad (13d)$$

$$T_{\text{mid}}^4 = \left(\frac{3}{8} \tau + \frac{1}{2} + \frac{1}{4\tau} \right) T_{\text{eff}}^4, \quad (13e)$$

$$\tau = \frac{\kappa \Sigma}{2}, \quad (13f)$$

$$p_{\text{rad}} = \frac{\tau}{2} \sigma_{\text{SB}} T_{\text{eff}}^4, \quad (13g)$$

where we have used the approximation $p \approx p_{\text{rad}}$ because we will solve the relativistic equations only in radiation-dominated parts.

In the relativistic regime, the solution differs from the Newtonian self-similar solution as there is an additional characteristic radius, sonic point r_{cs} , where the inflow velocity surpasses the local sound speed (see next subsection for explicit definition of r_{cs}). Based on the observation that the outflow dies down around the characteristic radius (Yuan et al. 2012a,b; McKinney et al. 2014; Sadowski et al. 2014; Yang

et al. 2014; Takahashi et al. 2018), we formulate the prescription of inflow rate as

$$\begin{aligned} \dot{m}_{\text{in}}(r)B(r) &= \text{const} \quad (r \geq r_{\text{cs}}), \\ \dot{m}_{\text{in}}(r) &= \text{const} \quad (r < r_{\text{cs}}). \end{aligned} \quad (14)$$

with the relativistic Bernoulli parameter being $B = E - 1 + \frac{\Gamma}{\Gamma-1}Ec_s^2$.

2.3. Numerical solutions to the relativistic model

In practice, we solve the relativistic disk structure for $r \leq 10^3 m_{\bullet}$ and use the Newtonian solution for $r \in (10^3 m_{\bullet}, r_Q)$, where r_Q is the marginally stable radius [see Eq. (4)]. In order to numerically solve the relativistic disk structure, we reorganize the dynamical equations (with the aid of the constraint equations) as

$$\frac{\partial \Omega}{\partial r} = V \frac{r^4 \Omega_{\perp}}{\frac{2}{3} \alpha \gamma \gamma_{\phi} c_s^2 A^{3/2}} \left(L - \frac{\dot{m}_{\text{in},0}}{\dot{m}_{\text{in}}} L_0 - \frac{1}{\dot{m}_{\text{in}}} \int_{r_0}^r L \frac{d\dot{m}_{\text{in}}}{dr} dr \right), \quad (15)$$

$$\frac{\partial \ln |V|}{\partial \ln r} = \frac{\frac{\mathcal{A}}{c_s^2} - \frac{2\Gamma}{\Gamma+1} \left(\frac{\partial \ln \dots}{\partial \ln r} \right) + \frac{\Gamma-1}{\Gamma+1} \delta F}{\left(\frac{1}{1-V^2} \frac{V^2}{c_s^2} - \frac{2\Gamma}{\Gamma+1} \right)}, \quad (16)$$

$$\frac{\partial \ln c_s}{\partial \ln r} = \frac{-\frac{\mathcal{A}}{c_s^2} + \left(\frac{1}{1-V^2} \frac{V^2}{c_s^2} \right) \left(\frac{\partial \ln \dots}{\partial \ln r} \right) - \left(\frac{1}{1-V^2} \frac{V^2}{c_s^2} - 1 \right) \delta F}{\left(\frac{1}{1-V^2} \frac{V^2}{c_s^2} - \frac{2\Gamma}{\Gamma+1} \right) \frac{\Gamma+1}{\Gamma-1}}, \quad (17)$$

with

$$\delta F = \frac{2\pi r^2}{\dot{m}_{\text{in}} c_s^2} (F^+ - F^-),$$

$$\left(\frac{\partial \ln \dots}{\partial \ln r} \right) = \left(\frac{\partial \ln \dot{m}}{\partial \ln r} + \frac{\partial \ln \gamma_{\phi}}{\partial \ln r} + \frac{\partial \ln \Omega_{\perp}}{\partial \ln r} - \frac{\partial \ln \sqrt{\Delta}}{\partial \ln r} \right).$$

Eq. (16) is singular at the sonic point r_{cs} where the denominator of the right-hand side vanishes, while a physical solution must also have a vanishing numerator at the same radius $r = r_{\text{cs}}$. For a given inflow rate $\dot{m}_{\text{in}}(r)$ and a sonic point r_{cs} , solving the three equations above is an eigenvalue problem with the to-be-determined eigenvalue L_0 . To close the eigenvalue problem with three independent variables and one eigenvalue, we need to specify 4 boundary conditions, which we choose according to Narayan et al. (1997): vanishing numerator and denominator of Eq. (16) at the sonic point $r = r_{\text{cs}}$, matching c_s and Ω with their counterparts in the Newtonian self-similar solution at $r = 10^3 m_{\bullet}$. Starting with a guess solution, we solve the above eigenvalue problem using the relaxation method (Press et al. 2002), and update the inflow rate $\dot{m}(r)$ according to the prescription (14) every a few steps of relaxation. We finally obtain the converged solution $\{V(r), c_s(r), \Omega(r), L_0\}$ in the range $r \in (r_{\text{cs}}, 10^3 m_{\bullet})$. With the eigenvalue L_0 , we again solve the three dynamical equations from the horizon r_{H} to the sonic point r_{cs} using the

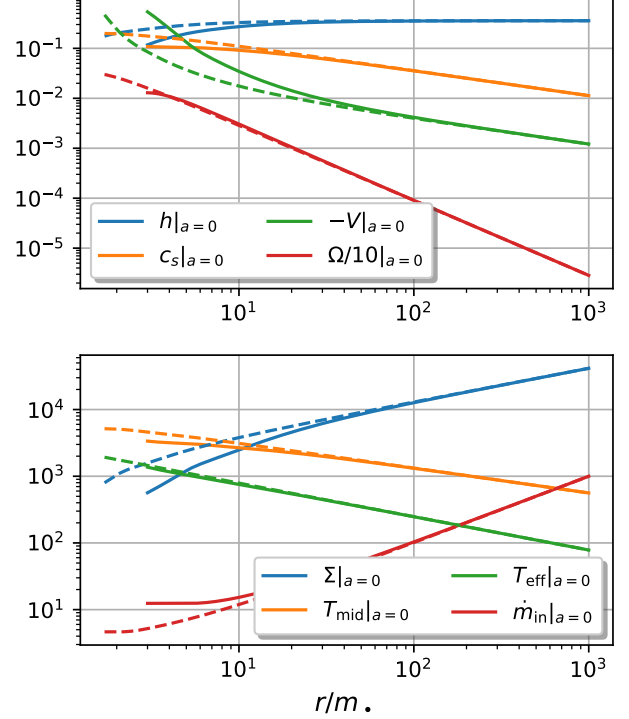


Figure 1. Numerical solutions to the supercritical inflow-outflow model. Solid/dashed lines are disk aspect ratio h , radial velocity V , sound speed c_s , angular velocity Ω [m_{\bullet}^{-1}], surface density Σ [g/cm^2], middle plane temperature T_{mid} [eV], effective temperature T_{eff} [eV], and gas inflow rate \dot{m}_{in} [$\dot{m}_{\bullet}^{\text{Edd}}$] for a BH with mass $m_{\bullet} = 10M_{\odot}$ and spin $a = 0/0.9$.

same relaxation method with 3 boundary conditions: vanishing numerator and denominator of Eq. (16) at $r = r_{\text{cs}}$, and $L = L_0$ at $r = r_{\text{H}}$. For an initial guess of r_{cs} , the two solution pieces generally do not match at $r = r_{\text{cs}}$. Therefore, we need to adjust the location r_{cs} of the sonic point and repeat the calculation above until a global solution is found.

In Fig. 1, we show two sample solutions with $m_{\bullet} = 10M_{\odot}$, $a = 0$ or 0.9 , $\dot{m}_{\text{in}} = 10^3 \dot{m}_{\bullet}^{\text{Edd}}$ at $r = 10^3 m_{\bullet}$ and $\alpha = 0.1$, where we have defined the Eddington accretion rate as $\dot{m}_{\bullet}^{\text{Edd}} = 10L_{\bullet}^{\text{Edd}}$, with the Eddington luminosity $L_{\bullet}^{\text{Edd}} = 1.26 \times 10^{38} (m_{\bullet}/M_{\odot})$ erg/s. Similar to slim disks (Sadowski 2009) and ADAFs (Abramowicz et al. 1996; Narayan et al. 1997), we find the sonic point location r_{cs} of the inflow-outflow model is also close to the innermost stable circular orbit (ISCO) r_{isco} regardless of the BH spin. As expected, both sample solutions approach the Newtonian self-similar solution for large r , and become increasingly different close to the BH. Compared to simulations of General Relativistic magnetohydrodynamics (GRMHD) (e.g., Sadowski et al. 2014), we find the simple steady inflow-outflow model reproduces the dependence of the disk structure on the BH spin a : as a increases, both the surface density $\Sigma(r)$ and the luminos-

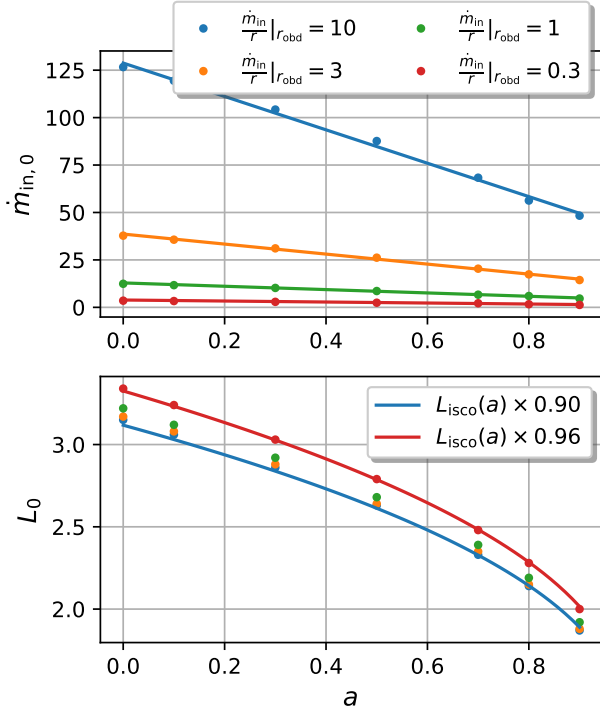


Figure 2. Upper panel: the BH accretion rate $\dot{m}_{in,0}$ [$\dot{m}_{in}^{Edd}/m_{\bullet}$] dependence on the BH spin a and the inflow rate at the outer boundary \dot{m}_{in}/r [$\dot{m}_{in}^{Edd}/m_{\bullet}$], where the discrete dots are numerical results and the solid lines are linear fitting of Eq. (18). Lower panel: the dependence of the specific angular momentum L_0 of gas falling into the horizon on the BH spin, where the two solid lines are $0.9L_{isco}(a)$ and $0.96L_{isco}(a)$, respectively.

ity (or equivalently the higher effective temperature $T_{eff}(r)$) grows, whereas the radial velocity $-V(r)$ and the specific angular momentum $L(r)$ decreases. The prescription for the inflow rate $\dot{m}_{in}(r)$ (Eq. 14) is well consistent with simulation results for large r , while the transition radius varies in different simulations (Yuan et al. 2012a,b; McKinney et al. 2014; Sądowski et al. 2014; Yang et al. 2014; Takahashi et al. 2018), and the choice of the sonic radius r_{cs} as the transition radius also reproduces its spin dependence found in these simulations.

We numerically solve the disk structure for different BH masses, spins, α values and inflow rates \dot{m}_{in} at the outer boundary $r_{obd} = 10^3 m_{\bullet}$. We find the dependence of the BH accretion rate $\dot{m}_{in,0}$ on the BH spin a and the inflow rate at the outer boundary can be well fitted by

$$\frac{\dot{m}_{in,0}}{\dot{m}_{in}^{Edd}} = (12.87 - 8.80a) \times \frac{\dot{m}_{in}(r_{obd})/r_{obd}}{\dot{m}_{in}^{Edd}/m_{\bullet}}, \quad (18)$$

and the specific angular momentum $L_0(a)$ and the specific energy $E_0(a)$ of gas falling into the horizon are approximated by $L_{isco}(a)$ and $E_{isco}(a)$ accurate to 10% or better, respectively, where $L_{isco}(a)$ and $E_{isco}(a)$ are the specific angular mo-

mentum and specific energy of particles on the ISCO $r_{isco}(a)$ (Bardeen et al. 1972), i.e.,

$$E_0(a) \approx E_{isco}(a) = \frac{r_{isco}^{3/2} - 2r_{isco}^{1/2} + a}{r_{isco}^{3/4} (r_{isco}^{3/2} - 3r_{isco}^{1/2} + 2a)}, \quad (19)$$

$$L_0(a) \approx L_{isco}(a) = \frac{r_{isco}^2 - 2ar_{isco}^{1/2} + a^2}{r_{isco}^{3/4} (r_{isco}^{3/2} - 3r_{isco}^{1/2} + 2a)}.$$

Note that both Eq. (18) and Eqs. (19) are independent of the BH mass m_{\bullet} and the α parameter. In Fig. 2, we show the numerical results of the BH accretion rate $\dot{m}_{in,0}$ and the specific angular momentum L_0 of gas falling into the horizon for $m_{\bullet} = 10M_{\odot}$ and $\alpha = 0.1$, along with the comparison to Eqs. (18,19).

2.4. Radiation efficiency of supercritical accretion and the EM counterpart of GW190521

As noted in previous studies (McKinney et al. 2014; Sądowski et al. 2014; Yang et al. 2014), the supercritical accretion is radiation inefficient in terms of radiation efficiency $\eta_{rad} := L_{rad}/\dot{m}_{in}(r_{obd}) = \int 2\pi r E F^{-} dr / \dot{m}_{in}(r_{obd})$. For the sample solution in Fig. 1 with spin $a = 0$, the disk luminosity $L_{rad} \approx 4.5L_{\bullet}^{Edd}$ whereas the mass inflow rate at the outer boundary is $10^3 \dot{m}_{in}^{Edd} = 10^4 L_{\bullet}^{Edd}$, therefore the radiation efficiency is $\eta_{rad} \approx 0.045\%$. For the other solution with spin $a = 0.9$, the disk luminosity is $L_{rad} \approx 5.2L_{\bullet}^{Edd}$ and the radiation efficiency is $\eta_{rad} \approx 0.052\%$.

Another interesting feature of the supercritical inflow-outflow model is that the disk luminosity is nearly independent of the inflow rate $\dot{m}_{in}(r_{obd})$ at the outer boundary, because both T_{mid}^4 and the optical depth τ are proportional to $\dot{m}_{in}(r_{obd})$, so that the effective temperature T_{eff} turns out to be nearly independent of $\dot{m}_{in}(r_{obd})$. In other words, the radiation cooling rate does not change because the disk becomes hotter (T_{mid}) and denser (τ) at the same time. As a result, the supercritical accretion becomes more advection dominated and more radiation inefficient for higher $\dot{m}_{in}(r_{obd})$. The radiation efficiency for $\dot{m}_{in}(r_{obd})/r_{obd} > \dot{m}_{in}^{Edd}/m_{\bullet}$ can be fitted as

$$\eta_{rad} \approx 0.5 \left(\frac{\dot{m}_{in}(r_{obd})}{\dot{m}_{in}^{Edd}} \right)^{-1}, \quad (20)$$

with mild dependence on the BH spin.

For comparison, the supercritical accretion of BHs without considering outflow has also been investigated by Beloborodov (1998), where the supercritical accretion is also found to be highly advection dominated. For accretion rate $\dot{m}_{\bullet} > 10\dot{m}_{\bullet}^{Edd}$, the radiation efficiency can be fitted as

$$\eta_{rad} \approx 0.18 \left(\frac{\dot{m}_{\bullet}}{\dot{m}_{\bullet}^{Edd}} \right)^{-0.7}, \quad (21)$$

with mild dependence on the BH spin. Therefore, the radiation efficiency of supercritical accretion (with or without outflow) is low and decreases with the accretion rate.

GW190521 is a merger of two BHs with masses of $\sim 85M_{\odot}$ and $\sim 66M_{\odot}$ (LIGO Scientific Collaboration & Virgo Collaboration 2020), and an optical flare with luminosity $\sim 10^{45}$ erg/s detected by Zwicky Transient Facility has been proposed as the EM counterpart of the merger (Graham et al. 2020). In Graham et al. (2020), the optical flare is interpreted as the emission from the Bondi-Hoyle-Lyttleton (BHL) accretion of the remnant BH in an AGN disk with accretion rate and luminosity

$$\begin{aligned} \dot{M}_{\text{BHL}} &= 2.8 \times 10^{25} \text{ g/s} \left(\frac{M_{\text{BBH}}}{100M_{\odot}} \right)^2 \left(\frac{v_{\text{rel}}}{100 \text{ km/s}} \right)^{-3} \\ &\times \left(\frac{\tilde{\rho}}{10^{-10} \text{ g/cm}^3} \right) \approx 2 \times 10^5 \dot{M}_{\bullet}^{\text{Edd}}, \quad (22) \\ L_{\text{rad}} &\approx 2.5 \times 10^{45} \text{ erg/s} \left(\frac{\eta_{\text{rad}}}{0.1} \right) \approx 2 \times 10^5 L_{\bullet}^{\text{Edd}}, \end{aligned}$$

where M_{BBH} is the mass of the remnant BH, $\tilde{\rho}$ is the local gas density in the AGN disk, v_{rel} is the relative velocity of the remnant BH w.r.t the local gas. However the assumed radiation efficiency $\eta_{\text{rad}} = 0.1$ largely overestimates the true value in the case of supercritical accretion (with or without outflow) with inflow rate as high as $2 \times 10^5 \dot{M}_{\bullet}^{\text{Edd}}$. In the supercritical inflow-outflow model, there is an upper limit of the disk luminosity $\lesssim 10L_{\bullet}^{\text{Edd}}$ as explained above, so that the luminosity will be orders of magnitude less than the level $\sim 2 \times 10^5 L_{\bullet}^{\text{Edd}}$ (see also McKinney et al. 2014; Sadowski et al. 2014; Yang et al. 2014). On the other hand, even in the supercritical accretion model without considering outflow, the radiation efficiency is about $\eta_{\text{rad}} \approx 3.5 \times 10^{-5}$ for $\dot{M}_{\text{BHL}} = 2 \times 10^5 \dot{M}_{\bullet}^{\text{Edd}}$. Therefore, the claimed optical flare seems unlikely to be explained by the emission from the supercritical accretion flow onto the remnant BH.

In fact, in the inflow-outflow model, most of the outflows are generated at radius comparable to r_{obd} , as inferred by the radius dependence of \dot{m}_{in} . As a result, these gas materials have not fully released the gravitational potential energy, as compared with the small fraction of gas that accretes onto the BH. In other words, the energy reservoir from the accretion flow roughly scales as $\dot{m}_{\text{in}}(r_{\text{obd}})/r_{\text{obd}}$, which is insufficient to power the proposed optical flare in Graham et al. (2020).

3. EVOLUTION OF SBHS IN AN AGN DISK

For a stellar cluster around an accreting MBH, some of stars and sBHs inside the cluster are captured by the disk, so that the total population settles into a cluster component and a disk component as interacting with the disk (Pan & Yang 2021). SBHs embedded in the AGN disk are expected to spin up and grow in mass via accretion as migrating toward the MBH. In this section, we will first introduce the commonly used AGN disk models, summarize the interactions of stars and sBHs with the AGN disk, then explore the mass and spin

evolution of the captured sBHs inside the disk and finally calculate their spatial distribution.

3.1. AGN disk models

The structure of AGN disks has not been fully understood due to two main uncertainties: the mechanism of disk angular momentum transport and the mechanism of disk heating in outer parts where the local viscosity heating is not sufficient. In this work, we consider three commonly used AGN disk models: α/β disk (Sirko & Goodman 2003) and TQM disk (Thompson et al. 2005). In the first two models, the disk momentum transport mechanism is characterized by the canonical disk viscosity, where the viscous stress is parameterized as $\alpha \tilde{p}/\alpha \tilde{p}_{\text{gas}}$ in the α/β disk model, with $\alpha \lesssim 1$ being a phenomenological parameter, \tilde{p} being the total pressure and \tilde{p}_{gas} being the gas pressure. In the outer parts of the disk, certain external heating process is assumed to keep the disk to be marginally stable against the disk self-gravity. In the TQM disk model, the disk angular momentum is assumed to be carried away by more efficient global torques and the gas inflow velocity is parameterized as a constant fraction of local sound speed i.e., $-\tilde{v}_r = X\tilde{c}_s$; in outer parts of the disk, star formation in the disk is self-consistently implemented to heat the disk and maintain its stability against the disk self-gravity.³ In this work, we use tilde variables to distinguish AGN disk variables from variables of small disks around stellar-mass objects.

In Fig. 3, we show the solutions in the three AGN disk models for a MBH with $M_{\bullet} = 4 \times 10^6 M_{\odot}$, $\dot{M}_{\bullet} = 0.1 \dot{M}_{\bullet}^{\text{Edd}}$, where we have used $\alpha = 0.1$ for the α/β disks and $X = 0.1$ for the TQM disk (see Pan & Yang 2021, for details). From Fig. 3, the α disk and the β disk become different from each other only at small \tilde{r} where the gas pressure becomes subdominant. This means that the viscous stress and the gas inflow velocity in the β disk become smaller than those in the α disk while the surface density becomes larger. One major difference of the solution of the TQM disk is that the gas inflow velocity is much higher than the value in the other two disks, therefore the surface density is much lower.

The α -viscosity prescription is known as a good approximation to the turbulence viscosity driven by magnetorotational instability in inner parts of accretion disks where the gas is fully ionized (Balbus & Hawley 1991, 1998; Martin et al. 2019). Therefore we expect α/β disk models should be a closer description to inner parts ($\tilde{r} \lesssim 10^5 M_{\bullet}$ for the disks in Fig. 3) of AGN disks in nature, while it is not clear which model works better in outer parts.

³ Very Recently, Gilbaum & Stone (2021) proposed a feedback-dominated accretion flow model in which outer parts of an AGN disk is heated by EM emissions from accreting sBHs embedded in the AGN disk.

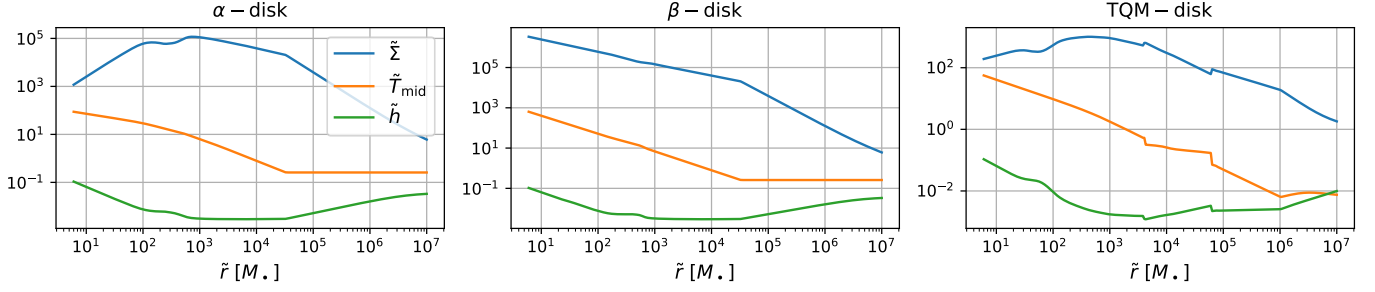


Figure 3. Three commonly used AGN disk models for a MBH with $M_{\bullet} = 4 \times 10^6 M_{\odot}$, $\dot{M}_{\bullet} = 0.1 \dot{M}_{\bullet}^{\text{Edd}}$, where $\alpha = 0.1$ for the α/β disk, and $X = 0.1$ for the TQM disk. The three disk variables shown are the disk surface density $\tilde{\Sigma}$ [g/cm^2], the disk middle-plane temperature \tilde{T}_{mid} [eV] and the disk aspect ratio \tilde{h} .

3.2. Density waves, head wind and supercritical accretion

Periodic motion of a sBH excites density waves that drive the inward migration of sBHs, circularize the planet’s orbit and drive the sBH orbit toward the disk plane (Goldreich & Tremaine 1979, 1980; Ward 1989; Tanaka et al. 2002; Tanaka & Ward 2004). Here we focus on the inward migration of a sBH in the AGN disk. Previous analytic studies together with numerical simulations show that the specific migration torque arising from density waves is given by (Tanaka et al. 2002; Tanaka & Ward 2004)

$$\dot{J}_{\text{mig,I}} = C_I \frac{m_{\bullet}}{M} \frac{\tilde{\Sigma}}{M} \frac{\tilde{r}^4 \Omega_{\bullet}^2}{\tilde{h}^2}, \quad (23)$$

where $M = M(< r)$ is the total mass within radius r , $C_I = -0.85 + d \ln \tilde{\Sigma} / d \ln \tilde{r} + 0.9 d \ln \tilde{T}_{\text{mid}} / d \ln \tilde{r}$ and Ω_{\bullet} is the angular velocity of the sBH around the MBH (Paardekooper et al. 2010).

Gas inside the influence sphere of the sBH tends to flow towards it. Due to the differential rotation of the disk, the nearly radial inflow at large separation, which generally carries nonzero angular momentum, becomes circularized at smaller separation. A disk consequently forms at the circularization radius, which serves as the outer boundary r_{obd} of the disk model. As described by the inflow-outflow model in the previous section, a large fraction of gas supplied at the outer boundary finally escapes in the form of outflow, and only the remaining part accretes onto the sBH. Because of the circularization process, it is reasonable to expect that the outflow carries minimal amount of net momentum w.r.t. the sBH. As a result, the “head wind” w.r.t the sBH are captured at places where the sBH gravity becomes important, and the momentum carried by the wind eventually transfers to the sBH. The specific torque exerted on the sBH from the wind is written as

$$\dot{J}_{\text{wind}} = -\frac{\tilde{r} \delta v_{\phi} \dot{m}_{\text{wind}}}{m_{\bullet}}, \quad (24)$$

where δv_{ϕ} is the relative bulk velocity in the ϕ direction. The head wind strength \dot{m}_{wind} (which determines the gas inflow rate $\dot{m}_{\text{in}}(r_{\text{obd}})$ of the sBH accretion disk at the outer boundary

r_{obd}) can be estimated according to the BHL rate \dot{m}_{BHL} with corrections accounting for the limit of MBH gravity in the radial direction and the finite size of the AGN disk in the vertical direction (Kocsis et al. 2011), i.e.,

$$\dot{m}_{\text{wind}} = \dot{m}_{\text{BHL}} \times \min \left\{ 1, \frac{\tilde{H}}{r_{\text{BHL}}} \right\} \times \min \left\{ 1, \frac{r_{\text{Hill}}}{r_{\text{BHL}}} \right\}, \quad (25)$$

and the circularization radius r_{cir} is estimated from the angular momentum conservation of infalling gas, i.e.,

$$\sqrt{r_{\text{cir}} m_{\bullet}} = v_{\text{rel}}(r_{\text{rel}}) r_{\text{rel}}, \quad (26)$$

with $r_{\text{rel}} := \min\{r_{\text{BHL}}, r_{\text{Hill}}\}$, \tilde{H} being the height of the AGN disk and $r_{\text{Hill}} = (m_{\bullet}/3M)^{1/3} \tilde{r}$ being the Hill radius of the sBH. The Bondi accretion rate and the Bondi radius are known as

$$\frac{\dot{m}_{\text{BHL}}}{m_{\bullet}} = \frac{4\pi \tilde{\rho} m_{\bullet}}{(v_{\text{rel}}^2 + \tilde{c}_s^2)^{3/2}}, \quad (27)$$

and $r_{\text{BHL}} = m_{\bullet}/(v_{\text{rel}}^2 + \tilde{c}_s^2)$, where v_{rel} is the relative velocity between the sBH and the local gas, $v_{\text{rel}}^2 = (\delta v_{\phi} + \delta v_{\text{dr}})^2 + \delta v_r^2$, with the relative bulk velocity δv_r in the r direction, and the relative velocity δv_{dr} coming from the differential rotation of the AGN disk (Kocsis et al. 2011):

$$\delta v_{\phi} = \frac{3 - \tilde{\gamma}}{2} \tilde{r} \tilde{h} \tilde{c}_s, \quad (28a)$$

$$\delta v_r = |\tilde{v}_{r,\text{gas}} - v_{r,\bullet}| = \left| -\frac{\dot{M}_{\bullet}}{2\pi \tilde{r} \tilde{\Sigma}} - \frac{\dot{J}}{dJ/d\tilde{r}} \right|, \quad (28b)$$

$$\delta v_{\text{dr}} = \frac{3}{2} \frac{r_{\text{rel}}}{\tilde{r}} \tilde{h}^{-1} \tilde{c}_s. \quad (28c)$$

Here $\tilde{\gamma}$ is defined as $d \ln \tilde{\rho} / d \ln \tilde{r}$, \dot{J} is the specific torque exerted on the sBH due to sBH-disk interactions and the GW emission, i.e., $\dot{J} = \dot{J}_{\text{mig,I,II}} + \dot{J}_{\text{wind}} + \dot{J}_{\text{gw}}$, where

$$\dot{J}_{\text{gw}} = -\frac{32}{5} \frac{m_{\bullet}}{M} \left(\frac{M}{\tilde{r}} \right)^{7/2}, \quad (29)$$

$\dot{J} = \tilde{r}^2 \Omega_{\bullet}$, $\dot{J}_{\text{mig,I,II}} = \dot{J}_{\text{mig,I}}$ or $\dot{J}_{\text{mig,II}}$, $\dot{J}_{\text{wind}} = \dot{J}_{\text{wind}}$ or 0 depending on whether a gap is opened. For later convenience,

we define the migration timescale of the sBH as

$$t_{\text{mig}} := \frac{\tilde{r}}{|\dot{\tilde{r}}|} = \frac{1}{2} \frac{J}{|\dot{J}|}. \quad (30)$$

For a sBH embedding in an AGN disk, the wind strength \dot{m}_{wind} and the circularization radius r_{cir} of inflowing gas are obtained from Eqs. (25-29). If the local disk around the sBH is stable against self-gravity at r_{cir} , i.e., $r_{\text{cir}} < r_Q$, the outer boundary conditions of the local disk are naturally

$$r_{\text{obd}} = r_{\text{cir}}, \quad \dot{m}_{\text{in}}(r_{\text{obd}}) = \dot{m}_{\text{wind}}. \quad (31)$$

On the other hand, if the local disk is unstable at r_{cir} , i.e., $r_{\text{cir}} > r_Q$, with gas feeding rate \dot{m}_{wind} , the gas inflow $\dot{m}_{\text{in}}(r_{\text{obd}})$ is consequently suppressed by the self-gravity instability until a larger marginally stable radius $r_Q \approx r_{\text{cir}}$ (which increases with decreasing accretion rate) is reached. Thus the boundary conditions are formulated as

$$r_{\text{obd}} = r_{\text{cir}}, \quad r_Q(\dot{m}_{\text{in}}(r_{\text{obd}})) = r_{\text{cir}}, \quad (32)$$

where $\dot{m}_{\text{in}}(r_{\text{obd}}) < \dot{m}_{\text{wind}}$.

With the above boundary conditions, the disk structure can be modelled and numerically solved as shown in the previous section. As a result, we obtain the sBH accretion rate as

$$\frac{\dot{m}_{\text{in},0}}{\dot{m}_{\bullet}^{\text{Edd}}} = \begin{cases} \dot{m}_{\text{in}}(r_{\text{obd}})/\dot{m}_{\bullet}^{\text{Edd}}, & (m_{\text{in}}(r_{\text{obd}}) < \dot{m}_{\bullet}^{\text{Edd}}) \\ \max\left\{(12.87 - 8.80\alpha) \frac{\dot{m}_{\text{in}}(r_{\text{obd}})/r_{\text{obd}}}{\dot{m}_{\bullet}^{\text{Edd}}/m_{\bullet}}, 1\right\}, & (\text{otherwise}) \end{cases} \quad (33)$$

following Eq. (18) and considering the possibility that the supercritical inflow-outflow model may not hold where the inflow rate \dot{m}_{in} falls below the Eddington rate, so that the disk description is switched to the one without outflow at subcritical rates. In the next subsection (Fig. 5), we will see this prescription of minimum sBH accretion rate has little impact on the mass and spin evolution of sBHs embedded in an AGN disk.

In Fig. 4, we show the sBH accretion rates $\dot{m}_{\text{in},0}$ and migration timescales t_{mig} of sBHs of mass $10M_{\odot}$ and zero spin, embedded in an AGN disk around a MBH of $4 \times 10^6 M_{\odot}$ (see Fig. 3). For all the three fiducial AGN disks, the migration timescale t_{mig} peaks at $\tilde{r} \sim 10^2 M_{\bullet}$, where \dot{J}_{gw} becomes comparable with $\dot{J}_{\text{mig},1} + \dot{J}_{\text{wind}}$. For the α disk case, $\dot{m}_{\text{in},0}$ also peaks at $\tilde{r} \sim 10^2 M_{\bullet}$ where the gas density $\tilde{\rho}$ peaks, while $\dot{m}_{\text{in},0}$ in the β disk is higher than that in the α disk due to higher gas density $\tilde{\rho}$ in the β disk. Among of the three, the gas density in the TQM disk is the lowest, inside which $\dot{m}_{\text{in},0}$ is also the lowest.

3.3. Mass and spin

In Section 3.2, we have outlined the calculation of the accretion rate of a sBH embedded in an AGN disk. Now we

consider the resulting mass and spin evolution:

$$\begin{aligned} dm_{\bullet} &= E_0(a) dm_{\text{gas}}, \\ d\mathcal{J}_{\bullet} &= L_0(a) m_{\bullet} dm_{\text{gas}} = \frac{L_0(a)}{E_0(a)} m_{\bullet} dm_{\bullet}, \end{aligned} \quad (34)$$

where dm_{gas} is the mass element of accreted gas, a fraction $1 - E_0(a)$ of which is converted to radiation escaping to infinity and the remaining fraction $E_0(a)$ is absorbed by the BH, and $\mathcal{J}_{\bullet} = am_{\bullet}^2$ is the sBH angular momentum. As a result, we obtain the following simple evolution equations for the mass and the spin

$$\begin{aligned} \dot{m}_{\bullet} &= E_0(a) \dot{m}_{\text{in},0}, \\ \dot{a} &= \left[\frac{L_0(a)}{E_0(a)} - 2a \right] \frac{\dot{m}_{\bullet}}{m_{\bullet}}. \end{aligned} \quad (35)$$

Together with Eq. (30), one can solve the migration and the mass and spin evolution of the sBH self-consistently in the AGN disk. In Fig. 5, we show the mass and spin evolution of sBHs for a duration 10^6 yr with initial mass $m_{\bullet,\text{ini}} = 5/10/20M_{\odot}$, initial spin $a_{\text{ini}} = 0$ and initial location $\tilde{r}_{\text{ini}} = 10^3 M_{\bullet}$. In the α disk and the β disk model, the sBHs have successfully migrated into the MBH in less than 10^6 yr and most of mass accumulation and spin amplification happen in the range of $\tilde{r} \lesssim 10^3 M_{\bullet}$, where both the migration timescale t_{mig} is relatively long and the sBH accretion rate $\dot{m}_{\text{in},0}$ is relatively high (see Fig. 4). In the TQM disk model, the mass accumulation and the spin increase of the sBH are much slower because of lower sBH accretion rate (see Fig. 4). Note that the TQM disk model is not expected to be a good description to inner parts ($\tilde{r} \lesssim 10^5 M_{\bullet}$ for the fiducial disks in Fig. 3) of AGN disks in nature, as explained in the beginning of Section 3, so we will focus on α and β disks in the following discussion.

3.4. Distribution of sBHs in the AGN disk

In this subsection, we focus on the density distribution of sBHs in inner parts of the AGN disk and all discussions here largely depend on our previous work (Pan & Yang 2021). We will find out how many sBHs are expected in the inner part of the disks where the mass and spin evolution of sBHs become more significant.

As sBHs and stars in the cluster orbiting around the accreting MBH, some of them are captured by the AGN disk and form a disk component. The statistical properties of cluster-component stars and sBHs are encoded in their distribution functions $f_i(t, \vec{x}, \vec{v})$ ($i = \text{star or bh}$). Following Refs. (Cohn & Kulsrud 1978; Cohn 1979), the distribution functions are approximately functions of the action variables, $f_i \approx f_i(t, E, R)$, with $E := \phi(\tilde{r}) - v^2/2$ being the specific binding energy (i.e., the positive potential energy minus the kinetic energy) and $R := J^2/J_c^2(E)$ being the normalized angular momentum, where J is the specific orbital angular momentum and

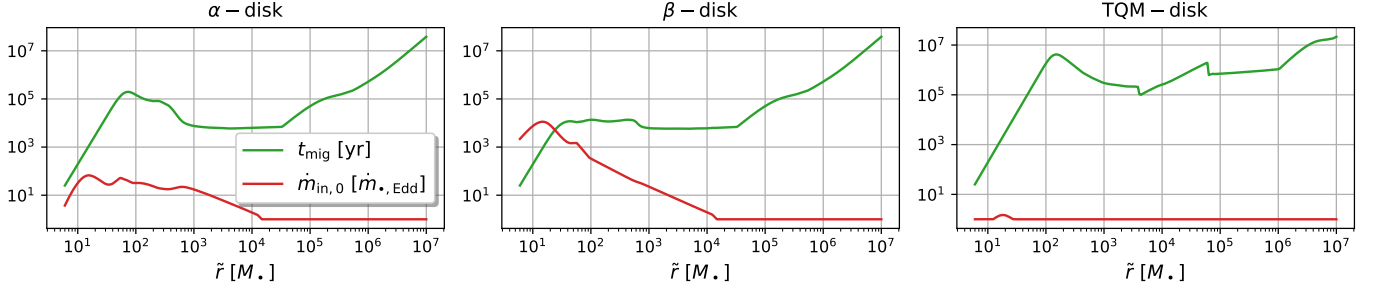


Figure 4. Migration timescales t_{mig} [Eq. (30)] and accretion rates $\dot{m}_{\text{in},0}$ [Eq. (33)] of SBHs with mass $m_{\bullet} = 10M_{\odot}$ and spin $a = 0$ embedded in fiducial AGN disks (Fig. 3).

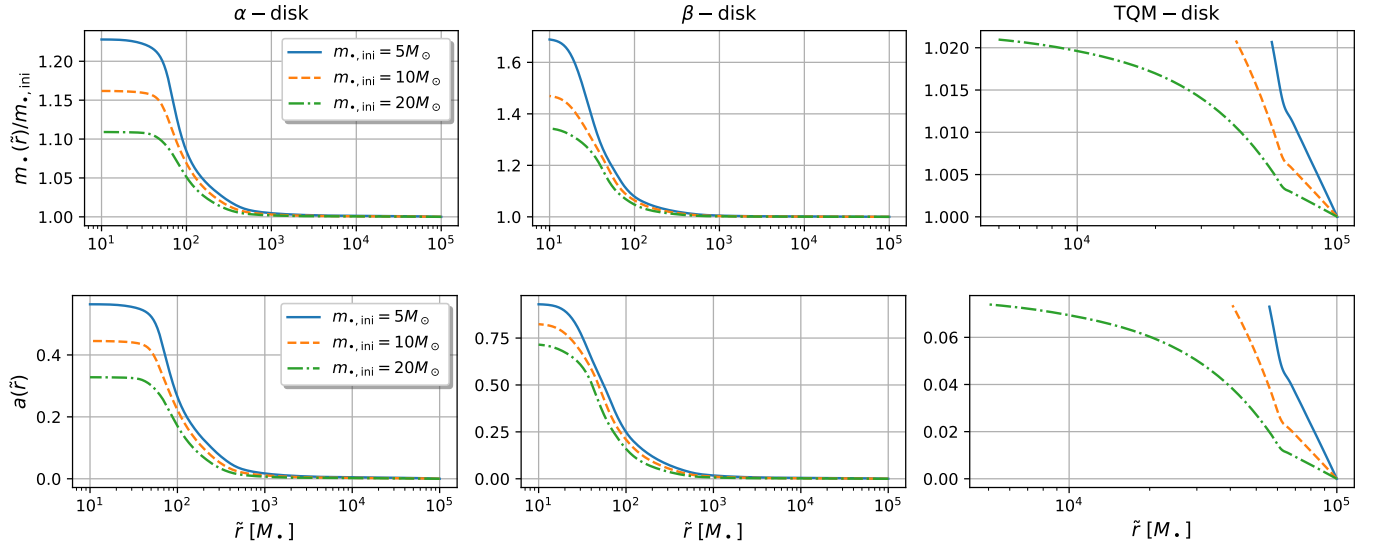


Figure 5. The mass and spin evolution of SBHs for a duration of 10^6 yr with initial mass $m_{\bullet,\text{ini}} = 5/10/20M_{\odot}$, initial spin $a_{\text{ini}} = 0$ and initial location $\tilde{r}_{\text{ini}} = 10^5 M_{\odot}$.

$J_c(E)$ is the specific orbital angular momentum of a circular orbiter with specific energy E . The distribution functions of cluster-component stars and SBHs are governed by the orbit-averaged Fokker-Planck equation (Pan & Yang 2021)

$$C \frac{\partial f}{\partial t} = -\frac{\partial}{\partial E} F_E - \frac{\partial}{\partial R} F_R + S, \quad (36)$$

where $C = C(E, R)$ is a normalization coefficient, $F_{E,R}$ is the flux in the E/R direction

$$\begin{aligned} -F_E &= \mathcal{D}_{EE} \frac{\partial f}{\partial E} + \mathcal{D}_{ER} \frac{\partial f}{\partial R} + \mathcal{D}_E f, \\ -F_R &= \mathcal{D}_{RR} \frac{\partial f}{\partial R} + \mathcal{D}_{ER} \frac{\partial f}{\partial E} + \mathcal{D}_R f, \end{aligned} \quad (37)$$

with the diffusion coefficients $\{\mathcal{D}_{EE}, \mathcal{D}_{RR}, \mathcal{D}_{ER}\}$, and the advection coefficients $\{\mathcal{D}_E, \mathcal{D}_R\}$ incorporating two-body scatterings in the cluster and interactions of stars and SBHs with the AGN disk. The (negative) source term S arises from stars

or SBHs captured by the disk, with

$$S_{\text{bh}} = -\mu_{\text{cap}} C \frac{f_{\text{bh}}}{t_{\text{mig}}^{\text{star}}} \frac{m_{\text{star}}}{m_{\text{bh}}}, \quad S_{\text{star}} = -\mu_{\text{cap}} C \frac{f_{\text{star}}}{t_{\text{mig}}^{\text{star}}}, \quad (38)$$

where μ_{cap} is a parameter quantifying the disk capture efficiency and we take $\mu_{\text{cap}} = 0.1$ as a fiducial value.

For SBHs in the AGN disk, the continuity equation is

$$\frac{\partial \Sigma_{\bullet}}{\partial t} + \frac{1}{\tilde{r}} \frac{\partial}{\partial t} (\tilde{r} \Sigma_{\bullet} v_{r,\bullet}) = \frac{1}{2\pi \tilde{r}} \int -S_{\text{bh}} \frac{dE}{d\tilde{r}} \Big|_{E=\phi(\tilde{r})/2} dR, \quad (39)$$

where Σ_{\bullet} is the surface number density of SBHs in the disk, $v_{r,\bullet} = \tilde{r}/t_{\text{mig}}$ [Eq. (30)] is the migration velocity in the radial direction, and the source term on the right-hand side comes from SBHs captured by the disk.

As an example, we consider a MBH with $M_{\bullet} = 4 \times 10^6 M_{\odot}$ hosting a stellar cluster consisting of $1M_{\odot}$ stars and $10M_{\odot}$ SBHs. We initialize the density profiles of stars and SBHs $n_{\text{star}}(r)$ and $n_{\bullet}(r)$ according to the Tremaine's cluster model

(Tremaine et al. 1994; Dehnen 1993) with the total star mass within the influence sphere of the MBH $\approx M_\bullet$ and the sBH number density is $n_\bullet(r) = 10^{-3}n_{\text{star}}(r)$. According to Soltan’s argument (Soltan 1982), the average total duration of AGN active phase is $\sim (10^7, 10^9)$ yr, MBHs should be quiet most of time. To mimic the AGN duty cycle, we evolve the system of the MBH+stellar cluster for $T_0 = 5$ Gyr without including of interactions of stars and sBHs with the disk, then turn on the disk influence and continue the evolution for a short time T_{disk} (see Pan & Yang 2021, for all the details of modelling and calculation).

The surface number density $\Sigma_\bullet(r)$ of sBHs captured in the disk is governed by the continuity equation (39). In Fig. 6, we show the surface number density Σ_\bullet of sBHs on the equator at the end of an AGN phase with duration $T_{\text{disk}} = 10^6/10^7/10^8$ yr. The total number of sBHs within radius \tilde{r}^* is related to the surface number density by $N_\bullet(< \tilde{r}^*) = \int_{< \ln \tilde{r}^*} 2\pi r^2 \Sigma_\bullet d \ln \tilde{r}$. In the α disk, we find $\approx (30 - 50)$ sBHs aggregate in the range $\tilde{r} < 10^3 M_\bullet$ at the end of an AGN phase as a result of a traffic jam.⁴ In the β disk, only $\approx (5 - 8)$ sBHs aggregate in this range where the migration timescale is much shorter than in the α disk.

Assuming the galactic MBH in Sgr A* went through an AGN phase that ended 10 Myrs ago (Levin & Beloborodov 2003), a number of sBHs should be brought to the vicinity of the MBH as shown above. If the masses of sBHs are close to $10M_\odot$, initially the closer ones ($\tilde{r} \lesssim 200M_\bullet$) should have been swallowed by the MBH as a result of GW emissions, while the remaining $\approx (2 - 12)$ sBHs are expected to be orbiting around the MBH today with radius $\tilde{r} < 10^3 M_\bullet$. These remaining sBHs may be promising monochromatic sources detectable by LISA.

4. EVOLUTION OF NEUTRON STARS AND WHITE DWARFS IN AN AGN DISK

4.1. Neutron stars

The supercritical accretion onto NSs is similar to that of BHs except with different inner boundary condition and possible effects from magnetic fields. For a BH, the inner boundary condition is naturally a no-torque condition on the horizon. For a NS, its magnetic field plays an important role, which has been investigated for decades in the context of NS accretion in X-ray binaries. The accretion disk of a NS is expected to be truncated where the magnetic pressure becomes dominant (King et al. 2016). The gas is accelerated or decelerated from approximately Keplerian angular velocity to

⁴ Gilbaum & Stone (2021) also found the aggregation of a very similar number of sBHs around the MBH in their feedback-dominated accretion flow of an accreting MBH of mass $10^7 M_\odot$ and accretion rate $0.1 M_\bullet^{\text{Edd}}$, though we have assumed different origins of sBHs embedded in the AGN disk: captured from the stellar cluster v.s. born in the AGN disk.

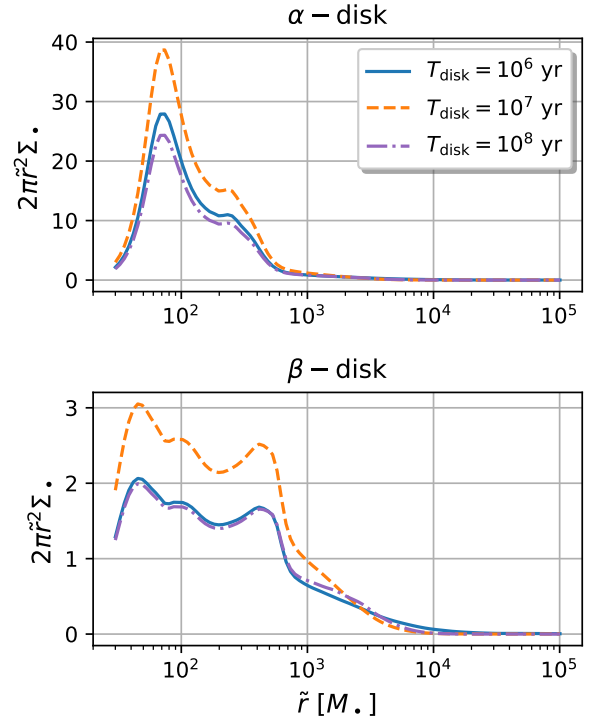


Figure 6. The surface number density $\Sigma_\bullet(\tilde{r} < 10^5 M_\bullet)$ of sBHs on the equator at the end of an AGN phase with duration T_{disk} .

the corotation angular velocity by the magnetic stress in a boundary layer between the magnetosphere and the undisturbed accretion disk, then flows along the field lines to the star surface (Ghosh & Lamb 1979a,b,c). On the other hand, the NS is either spun up or spun down as a result of the angular momentum gain from accreted gas and the angular momentum loss as magnetically interacting with the accretion disk.

As the surrounding gas accretes onto the NS, the magnetic fields near the star surface generally decays due to Ohmic dissipation in the heated crust, or being buried under a mountain of the accreted material or leading to the destruction of superconducting vortices in the core of the NS (see e.g., Bisnovatyi-Kogan & Komberg 1974; Konar & Bhattacharya 1997; Istomin & Semerikov 2016; Konar 2017). These mechanisms are proposed to explain the fact that recycled pulsars have substantially weaker surface magnetic fields ($\sim 10^{8-9}$ G) compared to young radio pulsars ($\sim 10^{11-13}$ G) (Manchester et al. 2005). In particular, in the Ohmic dissipation model, the NS magnetic field decays as the crust is heated up and the decay stops when the crust sinks into the superconducting core (Konar & Bhattacharya 1997). In other decay models, whether there is a mechanism to stop the field decay is not clear. In the following discussion, we adopt the Ohmic heating model and parameterize

the NS surface field evolution as

$$B_{\text{ns}}(t) = \max \left\{ B_{\text{ns,ini}} \frac{1}{1 + t/\tau}, B_{\text{ns,fin}} \right\}, \quad (40)$$

where τ is the decay timescale, and $B_{\text{ns,fin}}$ is final frozen field strength. For an NS accreting gas with Eddington accretion rate $\dot{m}_{\text{ns}}^{\text{Edd}}$, $\tau \approx 10^3$ yr and $B_{\text{ns,fin}} \approx (10^9 - 10^{10})$ G (Konar & Bhattacharya 1997).

In order to calculate the accretion rate \dot{m}_{ns} of a NS with mass m_{ns} and surface magnetic field B_{ns} and embedded in an AGN disk, we first numerically solve the supercritical inflow and outflow model assuming the background spacetime is Schwarzschild as in Section 2, then truncate the disk at radius r_{ibd} where the magnetic pressure equals the ram pressure (see Ghosh & Lamb 1979a,b,c, for more detailed calculation), and in practice we have

$$r_{\text{ibd}} = \max \left\{ r_{\text{ns}}, \xi \left(\frac{B_{\text{ns}}^4 r_{\text{ns}}^{12}}{2m_{\text{ns}} \dot{m}_{\text{in}}^2(r_{\text{ibd}})} \right)^{1/7} \right\}, \quad (41)$$

where r_{ns} is the NS radius, ξ is a factor of $\mathcal{O}(1)$ which we take as $\xi = 0.52$ following Ghosh & Lamb (1979c) and we have assumed a dipolar configuration of the NS magnetic field. Therefore the NS accretion rate is

$$\dot{m}_{\text{ns}} = \begin{cases} 0, & (r_{\text{ibd}} = r_{\text{ns}} \text{ and } \Omega_{\text{ns}}/\Omega_{\text{K}}(r_{\text{ns}}) > 1) \\ \max \{ \dot{m}_{\text{in}}(r_{\text{ibd}}), \dot{m}_{\text{ns}}^{\text{Edd}} \}, & (\text{otherwise}) \end{cases} \quad (42)$$

considering that the accretion onto the star surface stops when the NS reaches the shedding limit with its angular velocity Ω_{ns} higher than the Keplerian angular velocity $\Omega_{\text{K}}(r_{\text{ns}})$ on the NS surface, and that the supercritical inflow-outflow model may not hold where the inflow rate falls below the Eddington rate (see Fig. 1 and Section 2). The magnetic field expands the effective size of the NS (if $r_{\text{ibd}} > r_{\text{ns}}$) and therefore accelerates its accretion.

The mass and spin evolution of the magnetized NS depends on the ratio of the NS angular velocity over the disk Keplerian angular velocity at the inner boundary, $\omega_{\text{ns}} := \Omega_{\text{ns}}/\Omega_{\text{K}}(r_{\text{ibd}})$. In the extreme propeller regime ($\omega_{\text{ns}} \gg 1$), accretion onto the NS is hindered by the centrifugal barrier and the NS is spun down as interacting with the accretion disk via the magnetosphere (Ghosh & Lamb 1979a,b,c). In the accretion regime ($\omega_{\text{ns}} < 1$), the NS is spun up by gas accretion. The equilibrium is reached at $\omega_{\text{ns}} \approx 1$. Following Ghosh & Lamb (1979c) and Dai & Li (2006), we assume the accretion onto the NS is not hindered abruptly in the mild propeller regime, and the total torque on the NS is

$$\frac{dJ_{\text{ns}}}{dt} = T_{\text{acc}} + T_{\text{mag}}, \quad (43)$$

where $J_{\text{ns}} = \frac{2}{5} m_{\text{ns}} r_{\text{ns}}^2 \Omega_{\text{ns}}$. There are various prescriptions of the accretion torque carried by gas falling onto the NS T_{acc}

and the magnetic torque T_{mag} exerted on the NS by the accretion disk exterior to the boundary layer. As modelled by Ghosh & Lamb (1979a,b,c), the accretion torque is

$$T_{\text{acc}}^{(1)} = T_0 := \dot{m}_{\text{ns}} \sqrt{m_{\text{ns}} r_{\text{ibd}}}, \quad (44)$$

assuming all angular momentum of gas at the inner boundary is absorbed by the NS, and the total torque is fitted as

$$T_{\text{acc}}^{(1)} + T_{\text{mag}}^{(1)} = T_0 \frac{1.39}{1 - \omega_{\text{ns}}} \times \left\{ 1 - \omega_{\text{ns}} \left[4.03(1 - \omega_{\text{ns}})^{0.173} - 0.878 \right] \right\}. \quad (45)$$

In a revised model (Dai & Li 2006), they are formulated as

$$T_{\text{mag}}^{(2)} = \frac{B_{\text{ns}}^2 r_{\text{ns}}^6}{r_{\text{ibd}}^3} \begin{cases} \frac{\xi^{7/2}}{3} \left(1 - 2\omega_{\text{ns}} + \frac{2}{3}\omega_{\text{ns}}^2 \right), & (\omega_{\text{ns}} \leq 1) \\ \frac{\xi^{7/2}}{3} \left(\frac{2}{3\omega_{\text{ns}}} - 1 \right), & (\omega_{\text{ns}} > 1) \end{cases} \quad (46)$$

$$T_{\text{acc}}^{(2)} = \begin{cases} T_0(1 - \omega_{\text{ns}}), & (r_{\text{ibd}} > r_{\text{ns}}) \\ T_0, & (r_{\text{ibd}} = r_{\text{ns}}) \end{cases}$$

assuming only part of the gas angular momentum is transferred to the NS via the interaction between magnetic fields and the gas in the boundary layer. The equilibrium state is reached at $\omega_{\text{ns}} = 0.35$ in the first prescription, and at $\omega_{\text{ns}} = 0.88$ in the second.

We consider the evolution of NSs in an AGN with initial mass $m_{\text{ns,ini}} = 1.4M_{\odot}$, radius $r_{\text{ns}} = 13$ km, initial location $\tilde{r}_{\text{ini}} = 10^5 M_{\bullet}$ and initial surface magnetic field $B_{\text{ns,ini}} = 10^{12}$ G. We also take $\tau = 10^3$ yr and $B_{\text{ns,fin}} = 10^{10}$ G or 10^9 G to mimic the field decay in the Ohmic dissipation model (Konar & Bhattacharya 1997). We show the evolution in Figs. 7 and 8 with the two prescriptions of angular momentum exchange, respectively. In both the α disk and the β disk, it takes the NS slightly more than 10^6 yr to migrate from its initial location to the MBH, where the NS surface magnetic field decays from 10^{12} G to 10^{10} G in $\sim 10^5$ yr as migrating from $\tilde{r} = 10^5 M_{\bullet}$ to $10^4 M_{\bullet}$. Massive NSs are stable only if they are below the collapse limit which is $\approx (2.1 - 2.5)M_{\odot}$ depending on the NS rotation angular velocity (Rezzolla et al. 2018), and we simply assume a linear dependence

$$M_{\text{ns,max}}/M_{\odot} = 2.1 + 0.4\Omega_{\text{ns}}/\Omega_{\text{K}}(r_{\text{ns}}). \quad (47)$$

With the first prescription of angular momentum exchange (Eq. 45) and the fiducial α AGN disk, the strong magnetic field $B_{\text{fin}} = 10^{10}$ G always truncates the NS accretion flow and keeps the NS in a slow-rotation state with angular velocity $\Omega_{\text{ns}} \approx 0.35\Omega_{\text{K}}(r_{\text{ibd}})$, and the NS collapses with mass $\approx 2.2M_{\odot}$ and spinning frequency ≈ 200 Hz. For the weak frozen field strength case ($B_{\text{fin}} = 10^9$ G), the NS accrete rate is lower and the NS does not reach the collapse limit with final mass $\approx 1.8M_{\odot}$. In the fiducial β disk in which the gas density is higher than in the α disk, thus the NS accretion rate

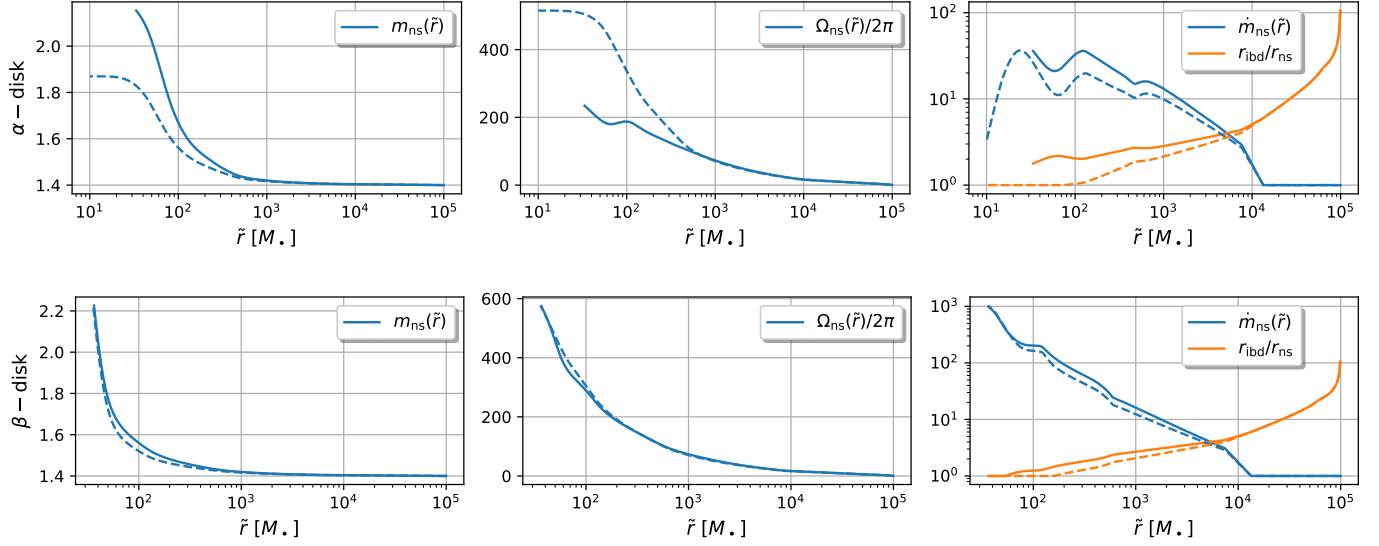


Figure 7. Mass and spin evolution of a NS embedded in an AGN disk assuming the first prescription (Eq. 45) of the angular momentum exchange. Upper row: the mass (left panel), spin frequency $\Omega_{\text{ns}}/2\pi$ [Hz] (middle panel), accretion rate \dot{m}_{ns} [$\dot{m}_{\text{ns}}^{\text{Edd}}$] and the inner radius the accretion disk r_{ibd} [r_{ns}] (right panel) of a NS in the fiducial α disk with initial mass $m_{\text{ini}} = 1.4M_{\odot}$ and initial position $\tilde{r}_{\text{ini}} = 10^5 M_{\odot}$, initial magnetic field $B_{\text{ns,ini}} = 10^{12}$ G, and finally frozen magnetic field $B_{\text{ns,fin}} = 10^{10}$ G (solid lines) or 10^9 G (dashed lines). Lower row: similar to the upper row except with the fiducial β disk.

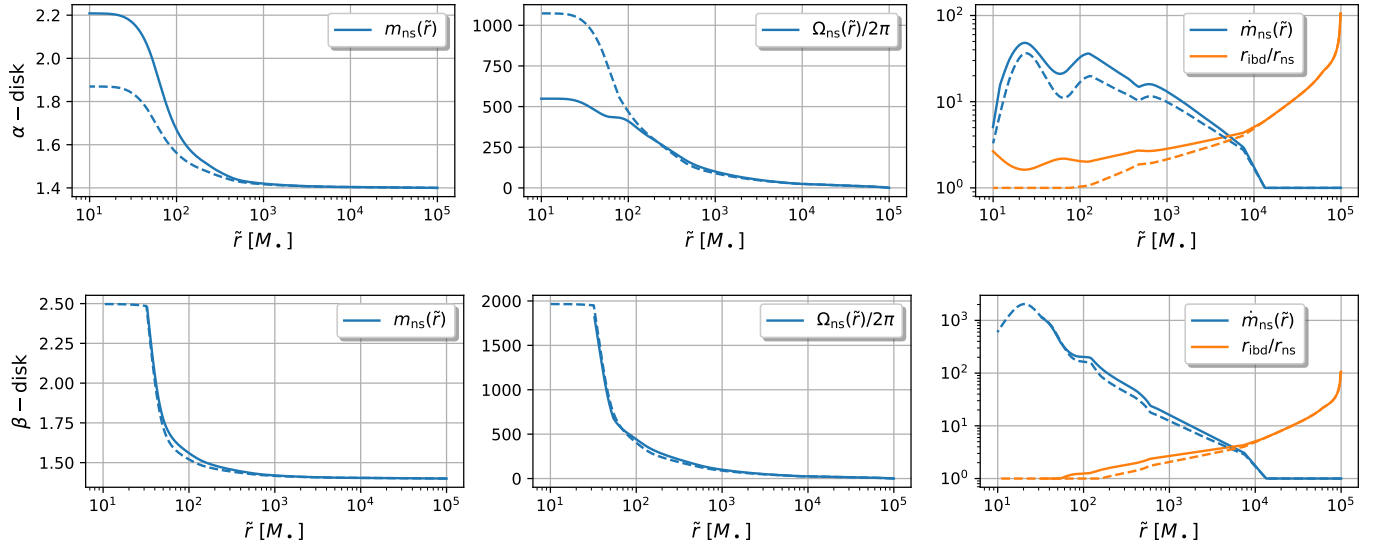


Figure 8. Similar to Fig. 7 except with the second prescription (Eq. 46) for the angular momentum exchange.

is also higher. As a result, the NS collapses with final mass $\approx 2.2M_{\odot}$ for either $B_{\text{fin}} = 10^{10}$ G or 10^9 G.

With the second prescription of angular momentum exchange (Eq. 46) and the fiducial α AGN disk, the strong magnetic field $B_{\text{fin}} = 10^{10}$ G again always truncates the NS accretion flow and keeps the NS rotating with a higher rate ($\Omega_{\text{ns}} \approx 0.88\Omega_{\text{K}}(r_{\text{ibd}})$) than in the first prescription and the NS finally grows to $\approx 2.2M_{\odot}$ but does not collapse because it is still below the spin-enhanced collapse limit. For the weak

frozen field strength case ($B_{\text{fin}} = 10^9$ G), the NS accretion rate is lower and the NS finally grows to $\approx 1.8M_{\odot}$ without collapse. In the fiducial β disk, the NS accretion rate is higher as explained in the previous paragraph. With the strong frozen magnetic field $B_{\text{fin}} = 10^{10}$ G, the NS grows to and collapses with mass $\approx 2.45M_{\odot}$ and nearly maximal spin ($\Omega_{\text{ns}} \approx 0.9\Omega_{\text{K}}(r_{\text{ns}})$). With the weak frozen magnetic field $B_{\text{fin}} = 10^9$ G, the NS accretion rate is lower while is spun up faster, thus the NS first reaches the shedding limit

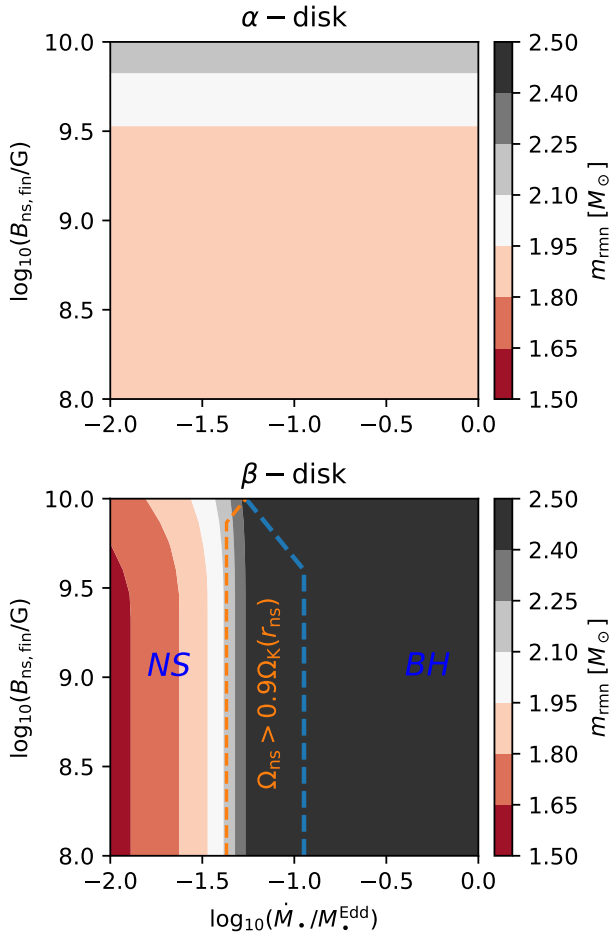


Figure 9. Final fates of NSs with initial mass $1.4M_{\odot}$, initial location $\tilde{r} = 10^5 M_{\bullet}$, in an AGN disk of a MBH of mass $M_{\bullet} = 4 \times 10^6 M_{\odot}$ and accretion rate \dot{M}_{\bullet} . For α disk model, the NS accretion rate is low, the NS does not grow to the collapse limit before merging with the central MBH. For β disk model with accretion rate $\dot{M}_{\bullet} \gtrsim 0.1\dot{M}_{\bullet}^{\text{Edd}}$, the NS accumulates sufficient mass and collapses with final mass $m_{\text{rnn}} \approx 2.5M_{\odot}$ (right side of the blue dashed line). For β disk model with accretion rate $\dot{M}_{\bullet} \lesssim 0.1\dot{M}_{\bullet}^{\text{Edd}}$, the NS does not collapse because its final mass is slightly below the spin-enhanced collapse limit (left side of the blue dashed line). Between the two dashed lines is the parameter space where the NS finally becomes a massive and fast rotating NS.

($\Omega_{\text{ns}} = \Omega_{\text{K}}(r_{\text{ns}})$) when the NS accretion is largely suppressed. As a result, the NS does not collapse with the final mass slightly below the maximal mass, which is $2.5M_{\odot}$ in our simple prescription.

We conclude this section by summarizing the final fate of a NS with initial mass $1.4M_{\odot}$ and zero initial spin, captured by an AGN disk around a MBH of mass $M_{\bullet} = 4 \times 10^6$ at radius $\tilde{r} = 10^5 M_{\bullet}$. As an illustrating example, we assume the prescription of angular momentum exchange (46). In Fig. 9, we show the influence of different AGN disk mod-

els, MBH accretion rates and the frozen NS magnetic field strength $N_{\text{ns,fin}}$. For α disk model in which the gas density is relatively low, the accretion rate is low so that the NS does not grow to the collapse limit before merging with the central MBH. For β disk model with accretion rate $\dot{M}_{\bullet} \gtrsim 0.1\dot{M}_{\bullet}^{\text{Edd}}$, the NS accumulates sufficient mass and collapses with final mass $m_{\text{rnn}} \approx 2.5M_{\odot}$. For lower accretion rate $\dot{M}_{\bullet} \lesssim 0.1\dot{M}_{\bullet}^{\text{Edd}}$, the NS does not collapse even if its final mass is marginally below the spin-enhanced collapse limit. To summarize, magnetic fields play an important role in the mass accumulation and spinning up of accreting NSs embedded in AGN disks: stronger magnetic fields lead to higher NS accretion rate and lower NS spinning rate, resulting in heavier NSs and easier NS collapses. The AGN disk structure, especially its gas density, also makes a big difference in the fate of NSs.

4.2. WDs

The evolution of WDs accreting gas from the stellar wind of a companion star has been extensively studied previously, which can give rise to very rich phenomena depending on the accretion rate (see e.g., Gallagher & Starrfield 1978; Fujimoto 1982; Iben 1982; Hachisu et al. 1996; Cassisi et al. 1998; Wolf et al. 2013; Chomiuk et al. 2020). A novae is ignited due to unstable burning of hydrogen on the WD surface if $\dot{m}_{\text{wd}} < \dot{m}_{\text{wd,stable}}$, where $\dot{m}_{\text{wd,stable}} \approx (2 \times 10^{-8} - 4 \times 10^{-7})M_{\odot}/\text{yr}$ depending on the WD mass is the minimal accretion rate for sustaining stable burning. For accretion rates slightly above $\dot{m}_{\text{wd,stable}}$, the stable hydrogen burning rate is equal to its accretion rate, so the WD continually accumulates mass until reaching the Chandrasekhar limit or the shedding limit. For even higher accretion rates $\gtrsim 3\dot{m}_{\text{wd,stable}}$, the hydrogen burning rate is lower than its accretion rate, thus the accreted hydrogen piles up on the WD surface as a radially expanding envelope (similar to that in red giants) until optically thick winds eventually slow down the net accretion.

We now examine the accretion rates of WDs placed in various locations of an AGN disk. Surface magnetic fields of WDs are generally weak ($< 10^5$ G) (Landstreet et al. 2012), therefore have little impact on the accretion flows of WDs. For a WD embedded in an AGN disk, the star accretion rate \dot{m}_{wd} is generally much higher compared with sBHs or NSs of similar mass because of its much larger size r_{wd} , with

$$\dot{m}_{\text{wd}} = \max \left\{ \dot{m}_{\text{in}}(r_{\text{obd}}) \times r_{\text{wd}}/r_{\text{obd}}, \dot{m}_{\text{wd}}^{\text{Edd}} \right\}. \quad (48)$$

In Fig. 10, we show the accretion rates of WDs with mass $m_{\text{wd}} = 0.5M_{\odot}$ and radius $r_{\text{wd}} = 10^4$ km, assuming the fiducial α AGN disk. For WDs located in a narrow annulus $\tilde{r} \approx 2 \times 10^6 M_{\bullet}$, their accretion rates fall in the stable hydrogen burning regime $(1 - 3)\dot{m}_{\text{wd,stable}} \approx (2 - 6) \times 10^{-8}M_{\odot}/\text{yr}$ (for $m_{\text{wd}} = 0.5M_{\odot}$) (Wolf et al. 2013). For WDs located exterior to this annulus, their accretion rates is lower than $\dot{m}_{\text{wd,stable}}$, thus these WDs do not grow because accumulated

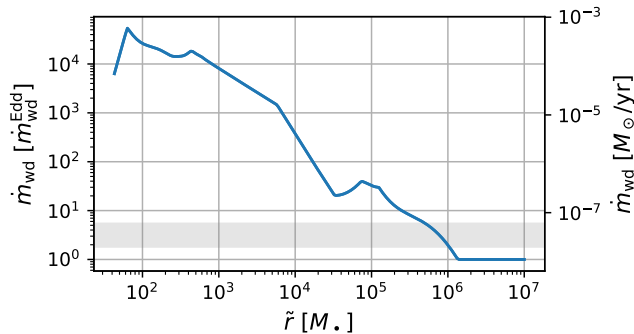


Figure 10. Accretion rates of WDs with mass $m_{\text{wd}} = 0.5M_{\odot}$ and radius $r_{\text{wd}} = 10^4$ km, located at different radii in the fiducial α AGN disk. The gray band is the stable burning regime where the hydrogen burning rate matches the accretion rate.

mass is blown away during novae eruptions. For WDs located at $\tilde{r} < 10^6 M_{\odot}$, the accretion rates are above $3\dot{m}_{\text{wd,stable}}$, and the accreted gas piles up on the WD surface causing an expanding red-giant-like structure with $r_{\text{rg}} \gg r_{\text{wd}}$. In a short period of time $\delta t \ll m_{\text{wd}}/\dot{m}_{\text{wd}}$, the “red giant” is spun up to the shedding limit $\sqrt{m_{\text{wd}}/r_{\text{rg}}^3}$ and the accretion stops. Therefore it seems difficult for WDs embedded in AGN disks to grow to the Chandrasekhar limit via accretion. This picture is also true for other two AGN disk models.

5. SUMMARY

AGN accretion disks have been proposed as promising sites for producing both mergers of stellar-mass compact objects and extreme mass ratio inspirals. For compact objects captured into an AGN disk, gas accretion generically happens and affects the long-term evolution of these objects, which has not been thoroughly understood and discussed in previous studies. In this paper, we construct a relativistic supercritical inflow-outflow model of BHs, based on previous Newtonian models and GRMHD simulations. In this model, the gas inflow rate $\dot{m}_{\text{in}}(r)$ is an increasing function of radius r because of the existence of outflows. Apart from having radius-dependent inflow rates, inflows in this model are very similar to canonical ADAFs (Narayan & Yi 1994; Narayan et al. 1997), both of which are radiation inefficient and advection dominated. As an application, we considered the speculated EM counterpart of GW190521, an optical flare of luminosity $\sim 10^{45}$ erg/s, which has been interpreted as the radiation from supercritical accretion of the remnant BH of mass $\sim 10^2 M_{\odot}$ in an AGN disk with an Bondi accretion rate $\approx 2 \times 10^5 \dot{M}_{\text{BBH}}^{\text{Edd}}$ and an radiation efficiency $\eta_{\text{rad}} \approx 0.1$ (Graham et al. 2020). There is an upper limit of the disk luminosity $\lesssim 10L_{\text{Edd}}$ in the supercritical inflow-outflow model, which

admits no solution to such high luminosity. To avoid possible model bias, we also invoke the model of supercritical accretion without outflow (Beloborodov 1998), which admits a much lower radiation efficiency $\eta_{\text{rad}} \approx 3.5 \times 10^{-5}$ (Eq. 21). Together with the energy argument, we conclude that the supercritical accretion onto the remnant BH seems unlikely to be the origin of such a bright optical flare.

We have applied the supercritical inflow-outflow model to study the evolution of sBHs embedded in AGN disks. For such a sBH, surrounding gas within its gravitational influence spheres tends to flow toward it, then circularizes and forms a disk-like profile due to non-zero angular momentum carried by the gas w.r.t the sBH. The outer boundary r_{obd} and the gas inflow rate at the outer boundary $\dot{m}_{\text{in}}(r_{\text{obd}})$ are specified by the circularization radius and the Bondi accretion rate with environmental corrections, respectively. We find that the inflow rate at the outer boundary $\dot{m}_{\text{in}}(r_{\text{obd}})$ is in general highly super-Eddington, while the sBH accretion rate $\dot{m}_{\ast,0}$ is only a small portion of $\dot{m}_{\text{in}}(r_{\text{obd}})$, which turns out to be mildly super-Eddington in most cases. As a result, the majority of sBHs that are captured onto the AGN disk and migrate into the MBH within the AGN disk lifetime only grow by a small fraction due to accretion.

We also applied the supercritical inflow-outflow model on studying NSs and WDs in AGN disks, taking into account corrections from star sizes and star magnetic fields. Accretion rates of embedded WDs rates are usually higher than that of BHs of similar mass because of much larger star sizes. However, WDs are spun up more efficiently to the shedding limit when the accretion onto star surface ceases because of angular momentum barrier, therefore it is hard for WDs to grow to the Chandrasekhar limit via accretion. For NSs, the surface magnetic fields may play an important role in both spinning up and accelerating the accretion. If NS magnetic fields are sufficiently strong to guide the accretion flow outside the NS surface and consequently keep the NS in a slow rotation state while accreting gas, it is possible for NSs to grow to the collapse limit via accretion. This opens up possibilities to form mass-gap-EMRIs that are detectable by LISA, whose event rate requires a separate study.

ACKNOWLEDGEMENTS

Z.P. and H.Y. are supported by the Natural Sciences and Engineering Research Council of Canada and in part by Perimeter Institute for Theoretical Physics. Research at Perimeter Institute is supported in part by the Government of Canada through the Department of Innovation, Science and Economic Development Canada and by the Province of Ontario through the Ministry of Colleges and Universities.

REFERENCES

- Abramowicz, M. A., Chen, X. M., Granath, M., & Lasota, J. P. 1996, *ApJ*, 471, 762
- Ashton, G., Ackley, K., Magaña Hernandez, I., & Piotrkowski, B. 2020, arXiv e-prints, arXiv:2009.12346
- Balbus, S. A., & Hawley, J. F. 1991, *ApJ*, 376, 214
- . 1998, *Reviews of Modern Physics*, 70, 1
- Banerjee, S., Baumgardt, H., & Kroupa, P. 2010, *MNRAS*, 402, 371
- Bardeen, J. M., Press, W. H., & Teukolsky, S. A. 1972, *ApJ*, 178, 347
- Bartos, I., Kocsis, B., Haiman, Z., & Márka, S. 2017, *ApJ*, 835, 165
- Begelman, M. C. 2012, *MNRAS*, 420, 2912
- Belczynski, K., Kalogera, V., & Bulik, T. 2002, *ApJ*, 572, 407
- Beloborodov, A. M. 1998, *MNRAS*, 297, 739
- Bisnovatyi-Kogan, G. S., & Komberg, B. V. 1974, *Soviet Ast.*, 18, 217
- Blandford, R. D., & Begelman, M. C. 1999, *MNRAS*, 303, L1
- . 2004, *MNRAS*, 349, 68
- Bonga, B., Yang, H., & Hughes, S. A. 2019, *Phys. Rev. Lett.*, 123, 101103
- Cassisi, S., Iben, I., & Tornambè, A. 1998, *ApJ*, 496, 376
- Chomiuk, L., Metzger, B. D., & Shen, K. J. 2020, arXiv e-prints, arXiv:2011.08751
- Cohn, H. 1979, *ApJ*, 234, 1036
- Cohn, H., & Kulsrud, R. M. 1978, *ApJ*, 226, 1087
- Dai, H. L., & Li, X. D. 2006, *A&A*, 451, 581
- Dehnen, W. 1993, *MNRAS*, 265, 250
- Fujimoto, M. Y. 1982, *ApJ*, 257, 767
- Gallagher, J. S., & Starrfield, S. 1978, *ARA&A*, 16, 171
- Ghosh, P., & Lamb, F. K. 1979a, *ApJ*, 232, 259
- . 1979b, *ApJ*, 234, 296
- . 1979c, *ApJ*, 234, 296
- Gilbaum, S., & Stone, N. C. 2021, arXiv e-prints, arXiv:2107.07519
- Goldreich, P., & Tremaine, S. 1979, *ApJ*, 233, 857
- . 1980, *ApJ*, 241, 425
- Graham, M. J., Ford, K. E. S., McKernan, B., et al. 2020, *PhRvL*, 124, 251102
- Hachisu, I., Kato, M., & Nomoto, K. 1996, *ApJL*, 470, L97
- Hurley, J. R., Tout, C. A., & Pols, O. R. 2002, *MNRAS*, 329, 897
- Iben, I., J. 1982, *ApJ*, 259, 244
- Istomin, Y. N., & Semerikov, I. A. 2016, *MNRAS*, 455, 1938
- Kimura, S. S., Murase, K., & Bartos, I. 2021, arXiv e-prints, arXiv:2103.02461
- King, A. L., Tomsick, J. A., Miller, J. M., et al. 2016, *ApJL*, 819, L29
- Kocsis, B., Yunes, N., & Loeb, A. 2011, *PhRvD*, 84, 024032
- Konar, S. 2017, *Journal of Astrophysics and Astronomy*, 38, 47
- Konar, S., & Bhattacharya, D. 1997, *MNRAS*, 284, 311
- Landstreet, J. D., Bagnulo, S., Valyavin, G. G., et al. 2012, *A&A*, 545, A30
- Lee, H. M. 1995, *MNRAS*, 272, 605
- Leigh, N. W. C., Geller, A. M., McKernan, B., et al. 2018, *MNRAS*, 474, 5672
- Levin, Y., & Beloborodov, A. M. 2003, *Astrophys. J. Lett.*, 590, L33
- LIGO Scientific Collaboration, & Virgo Collaboration. 2020, *PhRvL*, 125, 101102
- . 2021, *Physical Review X*, 11, 021053
- Manchester, R. N., Hobbs, G. B., Teoh, A., & Hobbs, M. 2005, *AJ*, 129, 1993
- Martin, R. G., Nixon, C. J., Pringle, J. E., & Livio, M. 2019, *New Astronomy*, 70, 7
- McKernan, B., Ford, K. E. S., Kocsis, B., Lyra, W., & Winter, L. M. 2014, *MNRAS*, 441, 900
- McKernan, B., Ford, K. E. S., Lyra, W., & Perets, H. B. 2012, *MNRAS*, 425, 460
- McKernan, B., Ford, K. E. S., & O’Shaughnessy, R. 2020a, *MNRAS*, 498, 4088
- McKernan, B., Ford, K. E. S., O’Shaughnessy, R., & Wysocki, D. 2020b, *MNRAS*, 494, 1203
- McKernan, B., Ford, K. E. S., Bellovary, J., et al. 2018, *ApJ*, 866, 66
- McKernan, B., Ford, K. E. S., Bartos, I., et al. 2019, *ApJL*, 884, L50
- McKinney, J. C., Tchekhovskoy, A., Sadowski, A., & Narayan, R. 2014, *MNRAS*, 441, 3177
- Narayan, R., Kato, S., & Honma, F. 1997, *ApJ*, 476, 49
- Narayan, R., & Yi, I. 1994, *ApJL*, 428, L13
- Nitz, A. H., & Capano, C. D. 2021, *ApJL*, 907, L9
- Paardekooper, S. J., Baruteau, C., Crida, A., & Kley, W. 2010, *MNRAS*, 401, 1950
- Page, D. N., & Thorne, K. S. 1974, *ApJ*, 191, 499
- Palmese, A., Fishbach, M., Burke, C. J., Annis, J., & Liu, X. 2021, *ApJL*, 914, L34
- Pan, Z., Lyu, Z., & Yang, H. 2021, arXiv e-prints, arXiv:2104.01208
- Pan, Z., & Yang, H. 2021, *PhRvD*, 103, 103018
- Perna, R., Lazzati, D., & Cantiello, M. 2021a, *ApJL*, 906, L7
- Perna, R., Tagawa, H., Haiman, Z., & Bartos, I. 2021b, *ApJ*, 915, 10
- Portegies Zwart, S. F., & McMillan, S. L. W. 2000, *ApJL*, 528, L17
- Press, W. H., Teukolsky, S. A., Vetterling, W. T., & Flannery, B. P. 2002, *Numerical recipes in C++ : the art of scientific computing*
- Rezzolla, L., Most, E. R., & Weih, L. R. 2018, *ApJL*, 852, L25
- Rybicki, G. B., & Lightman, A. P. 1986, *Radiative Processes in Astrophysics*
- Sadowski, A. 2009, *ApJS*, 183, 171

- Sadowski, A., Narayan, R., McKinney, J. C., & Tchekhovskoy, A. 2014, *MNRAS*, 439, 503
- Secunda, A., Bellovary, J., Mac Low, M.-M., et al. 2019, *ApJ*, 878, 85
- . 2020, *ApJ*, 903, 133
- Shakura, N. I., & Sunyaev, R. A. 1973, *A&A*, 500, 33
- Sigurdsson, S., & Phinney, E. S. 1993, *ApJ*, 415, 631
- Sirko, E., & Goodman, J. 2003, *MNRAS*, 341, 501
- Soltan, A. 1982, *MNRAS*, 200, 115
- Stephan, A. P., Naoz, S., Ghez, A. M., et al. 2016, *MNRAS*, 460, 3494
- Stone, N. C., Metzger, B. D., & Haiman, Z. 2017, *MNRAS*, 464, 946
- Tagawa, H., Haiman, Z., Bartos, I., & Kocsis, B. 2020a, *ApJ*, 899, 26
- Tagawa, H., Haiman, Z., & Kocsis, B. 2020b, *ApJ*, 898, 25
- Tagawa, H., Kocsis, B., Haiman, Z., et al. 2021, *ApJ*, 908, 194
- Takahashi, H. R., Mineshige, S., & Ohsuga, K. 2018, *ApJ*, 853, 45
- Tanaka, H., Takeuchi, T., & Ward, W. R. 2002, *ApJ*, 565, 1257
- Tanaka, H., & Ward, W. R. 2004, *ApJ*, 602, 388
- Thompson, T. A., Quataert, E., & Murray, N. 2005, *ApJ*, 630, 167
- Tremaine, S., Richstone, D. O., Byun, Y.-I., et al. 1994, *AJ*, 107, 634
- Wang, J.-M., Liu, J.-R., Ho, L. C., & Du, P. 2021a, *ApJL*, 911, L14
- Wang, J.-M., Liu, J.-R., Ho, L. C., Li, Y.-R., & Du, P. 2021b, arXiv e-prints, arXiv:2106.07334
- Ward, W. R. 1989, *ApJ*, 336, 526
- Wolf, W. M., Bildsten, L., Brooks, J., & Paxton, B. 2013, *ApJ*, 777, 136
- Xie, F.-G., & Yuan, F. 2008, *ApJ*, 681, 499
- Yang, H., Bonga, B., Peng, Z., & Li, G. 2019, *Phys. Rev. D*, 100, 124056
- Yang, H., & Casals, M. 2017, *Phys. Rev. D*, 96, 083015
- Yang, X.-H., Yuan, F., Ohsuga, K., & Bu, D.-F. 2014, *ApJ*, 780, 79
- Yang, Y., Bartos, I., Haiman, Z., et al. 2020a, *ApJ*, 896, 138
- . 2019a, *ApJ*, 876, 122
- Yang, Y., Gayathri, V., Bartos, I., et al. 2020b, *ApJL*, 901, L34
- Yang, Y., Bartos, I., Gayathri, V., et al. 2019b, *PhRvL*, 123, 181101
- Yuan, F., Bu, D., & Wu, M. 2012a, *ApJ*, 761, 130
- Yuan, F., Wu, M., & Bu, D. 2012b, *ApJ*, 761, 129
- Yunes, N., Kocsis, B., Loeb, A., & Haiman, Z. 2011, *Phys. Rev. Lett.*, 107, 171103
- Zahra Zeraatgari, F., Abbassi, S., & Mosallanezhad, A. 2016, *ApJ*, 823, 92
- Zahra Zeraatgari, F., Mosallanezhad, A., Yuan, Y.-F., Bu, D.-F., & Mei, L. 2020, *ApJ*, 888, 86
- Zhu, J.-P., Wang, K., & Zhang, B. 2021a, arXiv e-prints, arXiv:2107.06070
- Zhu, J.-P., Wang, K., Zhang, B., et al. 2021b, *ApJL*, 911, L19
- Zhu, J.-P., Yang, Y.-P., Zhang, B., et al. 2021c, *ApJL*, 914, L19
- Zhu, J.-P., Zhang, B., Yu, Y.-W., & Gao, H. 2021d, *ApJL*, 906, L11